Chemical Engineering Science 211 (2020) 115289

Contents lists available at ScienceDirect

Chemical Engineering Science

journal homepage: www.elsevier.com/locate/ces

Modeling of inter- and intra-particle coating uniformity in a Wurster fluidized bed by a coupled CFD-DEM-Monte Carlo approach

Zhaochen Jiang [a,b,*], Christian Rieck [b], Andreas Bück [a], Evangelos Tsotsas [b]

[a] Institute of Particle Technology (LFG), FAU Erlangen-Nuremberg, Cauerstr. 4, 91058 Erlangen, Germany
[b] Thermal Process Engineering, Otto-von-Guericke University Magdeburg, Universitaetsplatz 2, 39106 Magdeburg, Germany

HIGHLIGHTS

- Modeling of Wurster coating by a coupled CFD-DEM-Monte Carlo approach.
- Prediction of intra- and inter-particle layer thickness and uniformity of porosity.
- Calculated residence time distributions are in accordance with PEPT measurement .
- Intra-particle layer thickness distribution agrees well with coating experiment.

GRAPHICAL ABSTRACT

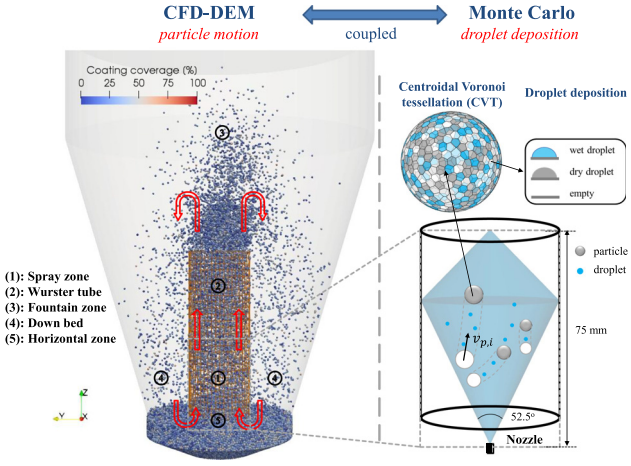

ARTICLE INFO

Article history:
Received 21 June 2019
Received in revised form 18 September 2019
Accepted 12 October 2019
Available online 16 October 2019

Keywords:
Coating
Surface coverage
Monte Carlo
CFD-DEM
Wurster fluidized bed

ABSTRACT

A coupled CFD-DEM and Monte Carlo approach was developed to investigate coating properties in a Wurster fluidized bed by considering gas flow, particle motion, droplet deposition, and the drying and solidifying of droplets on particle surfaces. Based on the spherical centroidal Voronoi tessellation (CVT), the Monte Carlo approach can model the deposition and splashing of spray droplets on the surface of individual particles. The capillary force induced by liquid bridges between particles was accounted in the DEM to investigate its influence on the coating and agglomeration behavior. The new model can provide information about the cycle time distribution, residence time distribution, coating coverage, uniformity of porosity (influenced by splashing) and layer thickness distributions on each individual particle (*intra-particle*) and in the particle population (*inter-particle*). The simulation results are compared with experimental data on residence time and intra-particle layer thickness distributions. Good agreement is observed between the simulation and the measurements.

1. Introduction

Coating of particulate materials is widely applied in the pharmaceutical, food, cosmetic, and fertilizer industries. In pharmaceutical applications, polymer-based film coating is critical to control

* Corresponding author at: Institute of Particle Technology (LFG), FAU Erlangen-Nuremberg, Cauerstr. 4, 91058 Erlangen, Germany.
E-mail address: zhaochen.jiang@fau.de (Z. Jiang).

https://doi.org/10.1016/j.ces.2019.115289
0009-2509/

Nomenclature

A	area [m^2]
A, B, C	dimensionless regression parameters in the capillary force [–]
d	diameter [m]
d_{inter}	inter-particle distance [m]
D_r	rupture distance [m]
e	coefficient of restitution [–]
E	Young's modulus [Pa]
F	normalized drag force [–]
$\boldsymbol{f}_{pf}$	particle–fluid interaction force (particle level, vector) [N]
$\boldsymbol{f}_c$	particle–particle interaction force (vector) [N]
$\boldsymbol{f}_{capillary}$	capillary force (vector) [N]
$\boldsymbol{f}_d$	drag force (vector) [N]
$\boldsymbol{F}_{pf}$	particle–fluid interaction force (cell level, vector) [N]
g	constant probability density function [–]
$\boldsymbol{g}$	acceleration due to gravity (vector) [m/s^2]
G	shear modulus [Pa]
h	layer thickness [m]
I	moment of inertia [kg $\cdot m^2$]
I_{A_c}	indicator function [–]
k	stiffness coefficient [N/m]
k_r	rolling coefficient [–]
L_{min}	minimum orthodromic distance [m]
m, M	mass [kg]
$\dot{m}$	drying rate [kg/(m^2·s)]
$\dot{M}$	mass flow rate [kg/s]
N_1	number of particles in interactions [–]
N_2	number of liquid bridges [–]
N_3	number of particles in a CFD cell [–]
N_{dep}	number of deposition panels [–]
N_p	number of particles in the bed [–]
$N_{p,MC}$	number of particles in Monte Carlo domain [–]
p	pressure [Pa]
r_1, r_2, r_3	random numbers in Monte Carlo simulations [–]
R	particle radius [m]
R_{ic}	number ratio of ideal to total cycles [–]
Re	Reynolds number [–]
s	cumulative sum of weights [–]
S_p	size of high porosity region [–]
Sc	Schmidt number [–]
Sh	Sherwood number [–]
$t, \Delta t$	time, time step [s]
T_t	tangential torque (vector) [N·s]
T_r	rolling torque (vector) [N·s]
$\boldsymbol{v}_p$	particle velocity (vector) [m/s]
$v_{c,max}$	maximum collision velocity [m/s]
v_{rel}	normal impact velocity between particle and droplet [m/s]
V	volume [m^3]
V_i	Voronoi region [–]
V_s	volume swept by moving particle [m^3]
We	Weber number [–]
x, y, z	Cartesian coordinates [m]
Y	moisture content of gas [kg H_2O/kg dry]

Greek symbols

α_d	damping ratio [–]
α_l	volume ratio of liquid bridge to two particles [–]
β	mass transfer coefficient of gas side [m/s)]
β_{pf}	momentum exchange coefficient [kg/(m^3 ·s)]
γ	droplet surface tension [N/m]
δ	diffusion coefficient between water and air [m^2/s]
ϵ	volume fraction, porosity [–]
ε	overlap between particles [m]
η	damping coefficient [(N·s)/m]
θ	contact angle [°]
μ_f	gas dynamic viscosity [Pa ·s]
μ_{fc}	friction coefficient [–]
ρ	density [kg/m^3]
σ	Poisson's ratio [–]
τ_H	Hertzian collision time [s]
$\boldsymbol{\tau}_f$	fluid stress tensor [Pa]
Ψ	coating coverage [–]
$\boldsymbol{\omega}$	particle angular velocity (vector) [rad/s]
$\boldsymbol{\omega}_r$	relative particle angular velocity (vector) [rad/s]

Subscripts

$1, 2$	different time steps
$2D$	two-dimensional space
A_c	start of a new cycle
c	coupling
con	conservative
d	droplet
dis	dissipative
eq	equivalent
f	fluid
g	gas
i, j, k	indices
l	liquid solution
m	Monte Carlo, mean
n	normal direction
p	particle
s	spray zone
sat	saturation
t	tangential direction, Wurster tube

Abbreviations

API	active pharmaceutical ingredient
CFD	computational fluid dynamics
CVT	centroidal Voronoi tessellation
CoV	coefficient of variation
DEM	discrete element method
HSD	Hertzian spring-dashpot
LBM	lattice Boltzmann method
MC	Monte Carlo
MCC	microcrystalline cellulose
PEPT	positron emission particle tracking
PBM	population balance modeling
RTD	residence time distribution

and prolong the release of active ingredients (Suzzi et al., 2010). For instance, minimum thickness and the absence of cracks of the functional coating film are required to protect the active pharmaceutical ingredient (API) against the acid environment in the stomach. Besides, the amount of API is directly correlated to the coating layer thickness in the active coating process. In the food industries, potential applications of coating include the protection of ingredients from the environment, the stabilization of the core during processing, the improvement of flowability and compression properties, and many more (Werner et al., 2007).

Spray fluidized beds and rotating drum (perforated pan) coaters are mainly used to conduct particle coating (Turton, 2008). The

Wurster fluidized bed is an efficient device for film coating of particles, which has been widely used to precisely coat pellets and pharmaceutical tablets in batch mode (Rajniak et al., 2009; Heinrich et al., 2015) or continuous mode (Hampel et al., 2013; Müller et al., 2019). The high gas velocity in the internal annulus generates pneumatic transport of particles in the Wurster tube, resulting in relatively narrow residence time distributions (RTDs) in the spray zone and the Wurster tube, respectively. Simultaneously, particles are wetted by droplets sprayed from a nozzle located on the distributor plate in the Wurster tube. After leaving the tube, the particles loose kinetic energy in the fountain zone and fall down to the outer bed region, where they are horizontally transported due to the low gas velocity in the external annulus. One circulation is completed when particles enter the spray zone again through the partition gap. In addition to imposing a circulation motion on the particles, the drying capacities of the gases in different regions can be adjusted to control the overall coating performance (Peglow et al., 2011; Bück et al., 2016).

The uniformity of the coating layer among particles (*inter-particle*) and on a single particle (*intra-particle*), the integrity, and the porosity of the coating layer are important attributes of the final product quality, especially in the pharmaceutical coating process. The end point and (average) coating layer thickness can be estimated. As reviewed by Knop and Kleinebudde (2013), experimental techniques to characterize coating attributes include visual imaging analysis, near infrared and Raman spectroscopy, terahertz pulsed imaging, and X-ray microtomography. Near-infrared and Raman spectroscopy rely on calibration models that require ongoing maintenance support. Sondej et al. (2015, 2016) investigated intra-particle coating layer morphology, the inter-particle coating thickness distribution and the porosity of coating layer by X-ray micro-computed tomography (μ-CT). By means of the same technique, Rieck et al. (2015) found a linear expression for the relationship between layer porosity and drying potential representing drying conditions in the fluidized bed. Laksmana et al. (2009) quantified the pore size distribution using confocal laser scanning microscopy. Schmidt et al. (2017) proposed a simple method to estimate layer porosity of particles coated with aqueous suspensions based on the size distribution (measured by a Camsizer, Retsch GmbH) and moisture content (measured by a drying oven) of particles before and after coating. Lin et al. (2017) reported the in-line measurement of intra-particle coating uniformity and inter-particle coating thickness distribution (in the range of 20 μm to above 300 μm) using combined terahertz and optical coherence tomography.

In addition to experiments, the discrete element method (DEM) is commonly used to predict the motion of particles in granular systems, due to its capabilities to simultaneously handle heat and mass transfer, cohesion force, non-spherical particles and poly-disperse particles. Coupling computational fluid dynamics (CFD) with DEM can be used to simulate particle–fluid systems in fluidized beds, cyclones, pneumatic conveying and channels (Zhou et al., 2010), involving non-spherical particles (Zhong et al., 2016a) and dense particulate system reactions (Zhong et al., 2016b). So far, most of CFD-DEM or DEM studies about wet coating and granulation processes investigated the residence time distributions (RTDs) in different zones of top-spray beds (Fries et al., 2011; Börner et al., 2017), Wurster coater, (Li et al., 2015b; Jiang et al., 2018a), prismatic shaped spouted bed (Fries et al., 2011), and high-shear wet granulator (Kulju et al., 2016). Then, RTDs can be used as the input parameters for macroscopic population balance modeling.

An essential part of wet particle formation processes is the generation of droplets by a nozzle (one or two-fluid), in which a liquid jet disintegrates into unstable sheets, then ligaments and finally droplets due to the combined effects of the turbulent (or cavitation) flow inside the nozzle, the high shear force induced by the interactions with the second fluid outside the nozzle, and the surface tension force and the viscosity force of the liquid (Hede et al., 2008; Poozesh et al., 2018). Owing to its great importance in environmental, chemical or medical applications and the inherently complex underlying physics, the modeling of the spraying and atomization process has always been at the leading edge of numerical simulations of multiphase flow (Jiang et al., 2010; Luo et al., 2019). Nevertheless, there is still no efficient numerical method to couple droplets into CFD-DEM accounting for the phenomena of, for instance, aggregation and breakage, the droplet deposition on particles, and drying and solidifying of droplets on particles or in the gas flow. As a common compromise, the droplets are treated as a type of solid discrete elements in CFD-DEM simulations, with the assumption that droplets are spherical, no aggregation and breakage occur, and certain simplified droplet coalescence and death criteria apply (Suzzi et al., 2010; Kieckhefen et al., 2019). Hilton et al. (2013) developed a method to map Stokesian solid-like droplets on individual particles based on the spherical harmonic formulation, which can predict the coating coverage and deposition volume at both intra-particle and inter-particle levels. The intra-particle coating variability of differently shaped particles was investigated by DEM simulations coupled with a graphical processing unit (GPU) based image analysis method in horizontal rotating pans (Freireich et al., 2015; Pei and Elliott, 2017). Specifically, as the particle appears in the predefined spray zone, the pixels in the image that are rendering the corresponding areas of the particles are considered to be coated. Askarishahi et al. (2017) used scalar transport equations to model the interaction between droplets and particles, and evaporation from the droplet in both, the spray and on the particle surface using an Euler–Lagrange approach. Moreover, the Monte-Carlo approach can be used to model particulate processes in which a sequence of discrete events, e.g., droplet deposition (Freireich and Wassgren, 2010; Rieck et al., 2016), aggregation of particles (Terrazas-Velarde et al., 2011; Rieck et al., 2016), and breakage of particles (Zhao et al., 2007; Zhang and You, 2015), are applied to the particle population.

Since the multi-scale coating process in fluidized bed is highly complex, it is often operated inefficiently in industrial applications. A new numerical approach is required to not only simulate multi-scale particle dynamics in fluidized beds, but also to directly predict coating layer uniformity of each individual particles. In this work, a coupled CFD-DEM-Monte Carlo approach was developed to study the inter- and intra-particle coating coverage and layer thickness distributions in a Wurster fluidized bed. The deterministic CFD-DEM method was used to predict the circulation motion of particles in different processing zones. Based on the particle positions and particle velocities obtained from CFD-DEM simulations, the stochastic Monte Carlo approach was used to model the deposition, the splashing and the drying of droplets on the surface of each individual particle. Then, variations of particle size due to deposition and drying were given back to the CFD-DEM solver. This new coupled approach can be used to manipulate coating morphology towards designed product properties in a real 3D Wurster fluidized bed by adjusting operation conditions of the system. The outline of this contribution is as follows. Section 2 gives a short description of the CFD-DEM method and the capillary force model. In addition, the models used in Monte Carlo to describe microscopic processes and events on individual particles are introduced. Section 3 presents and discusses simulation results of one case with cohesion forces in the DEM and one case without cohesion forces. Furthermore, detailed comparisons in terms of the residence time distribution, coating coverage and coating layer thickness are performed with experiment data and analytic models. Section 4 offers conclusions and outlook on further research.

2. Modeling methodology

2.1. CFD-DEM simulation

All models, boundary conditions, and numerical techniques used in CFD-DEM simulations were previously published. A short overview of the entire CFD-DEM method, including the governing equations for the solid particles and the gas phase (Zhou et al., 2010), the drag model for the particle–fluid momentum exchange (Beetstra et al., 2007a; Beetstra et al., 2007b), the Hertzian spring-dashpot contact model (soft-sphere) (Antypov and Elliott, 2011), the rolling model (Ai et al., 2011), and the cohesion model for capillary force (Soulié et al., 2006), is given in Appendix A. In comparison with experiments, this simulation method has been successfully used to predict the residence time distributions in a Wurster fluidized bed and the mixing behavior of poly-disperse particle systems in a pseudo-2D fluidized bed in our previous works (Jiang et al., 2018a; Jiang et al., 2018b).

To investigate the effect of cohesion forces on particle circulation in the Wurster bed, the capillary force induced by liquid bridge, Eq. (A.21), was also taken into account in the DEM simulation. The capillary force was related to the separation (inter-particle) distance d_{inter}, the surface tension of the liquid γ, and the dimensionless regression parameters A, B, C obtained from the solution of the Laplace-Young equation (Soulié et al., 2006). Liquid bridges appear if the inter-particle distance between two particles is shorter than the rupture distance D_r or during the collision of two particles. Note that the inter-particle distance was considered zero in the latter case, where the magnitude of capillary force had a constant value. Moreover, the capillary force disappears when the separation distance increases to the point of bridge rupture. When implementing the liquid bridge force model into DEM simulations, some assumptions are used: i) the capillary force only exists in the Wurster tube and spray zone; ii) the volume of all individual liquid bridges is equal and constant (without effects of drying and bridge rupture); and iii) there is no capillary force during particle–wall interactions. The parameter α_l, which defines the ratio of the volume of liquid bridge V_l and the total volume of two primary particles $2V_p$ (mono-disperse), was a model parameter to calculate the volume of liquid bridge.

2.2. Monte Carlo modeling

An overview of the integration of the Monte Carlo with CFD-DEM is given in Fig. 1. In each Monte Carlo time step Δt_m, one event of droplet deposition is guaranteed to occur on the single particle in the Monte Carlo domain. Particle dynamics in the CFD-DEM simulation are used in the stochastic Monte Carlo approach to model microscopic processes including deposition and splashing of droplets and drying of droplets, as shown in Fig. 2. The time step Δt_m can be calculated from the number flow rate of droplets sprayed into the spray zone, expressed by:

$$\Delta t_m = -\ln r_1 \left(\frac{6\dot{M}_l}{\pi \rho_d d_d^3} \right)^{-1} \tag{1}$$

where $\dot{M}_l$ is the mass flow rate of solution and r_1 is a uniformly distributed random number from the interval $\in (0, 1)$. The initial diameter of droplets d_d and mass density of droplets ρ_d are constant in the model. Once total Monte Carlo process time t_m becomes larger than $\Delta t_{c,2}$ (Table 1), the new particle diameters d_p are given back to the CFD-DEM solver; and the CFD-DEM simulation is conducted for another time period of duration $\Delta t_{c,2}$. Accordingly, the particles

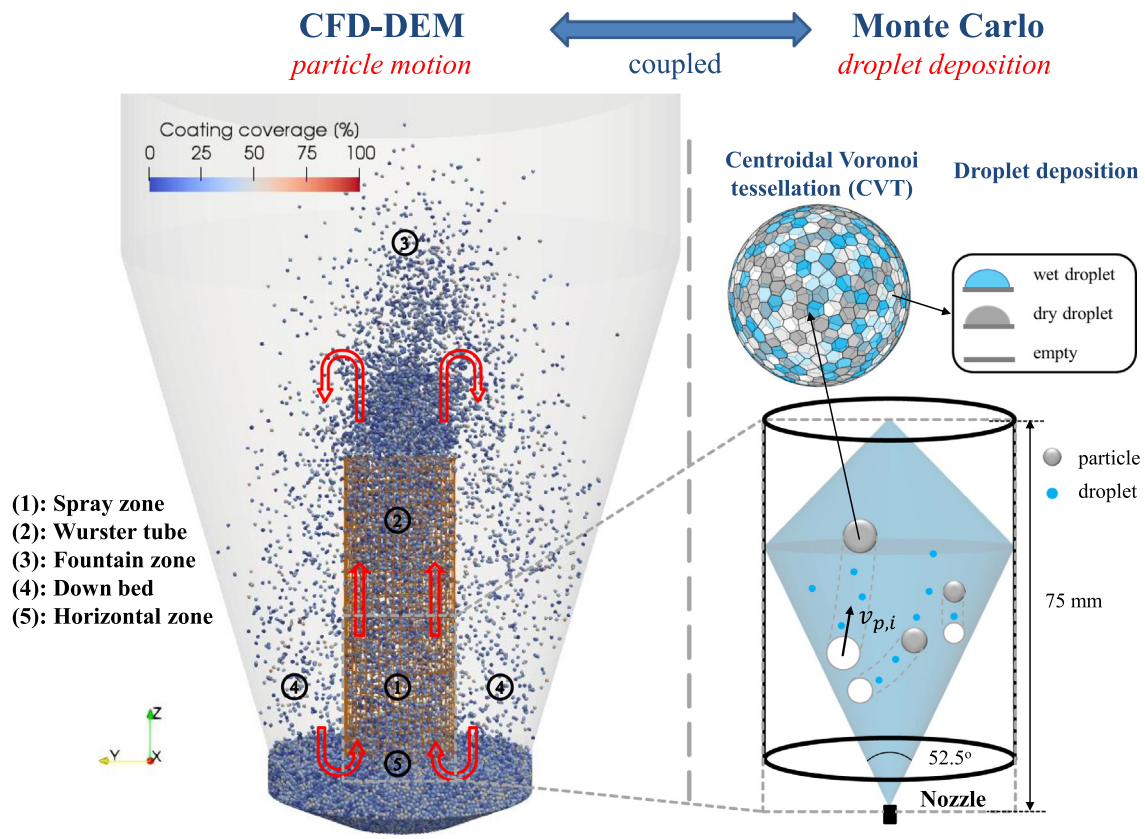

Fig. 1. Schematic of the coupled CFD-DEM-Monte Carlo approach for predicting coating of particles in the Wurster fluidized bed, including the macroscopic particle circulation motion in different zones and microscopic droplet deposition on the surface of individual particles in the spray zone.

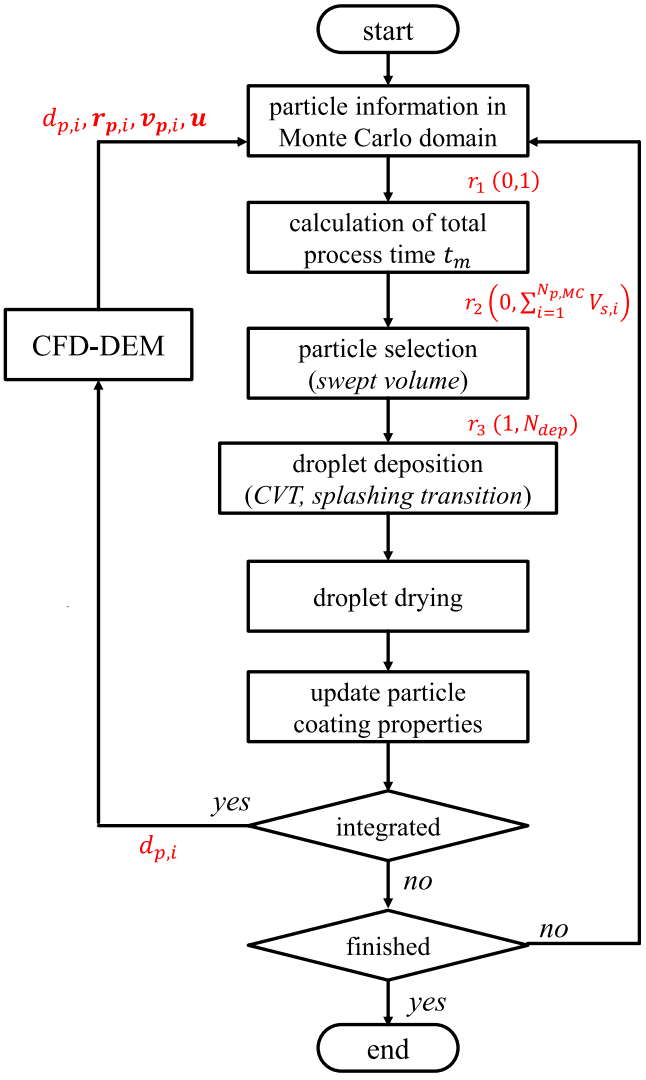

Fig. 2. Flowchart of the coupled CFD-DEM-Monte Carlo approach.

in the Monte Carlo domain are updated based on the new CFD-DEM data.

2.2.1. Particle selection

The Monte Carlo domain was set according to the geometry of the spray zone, as shown in Fig. 1. The number of particles in the Monte Carlo domain, $N_{p,MC}$, was evaluated from the positions of individual particles in CFD-DEM simulations.

The probability of particle i to receive liquid droplets was related to the volume swept by this moving particle in the spray zone, which can be calculated by $V_{s,i} = \pi(d_{p,i}/2 + d_d/2)^2 v_{p,i}\Delta t_m$. In other words, the particles were weighted by the swept volumes and the probability of each particle to be selected was determined by its relative weight. Fig. 3 shows a straightforward algorithm: 1) calculate the cumulative sum of weights for each particle $s(i) = \sum_i V_{s,i}$ (particles are arranged in a sequence of 1 to $N_{p,MC}$), 2) select a random number r_2 from the interval $(0, \sum_{i=1}^{N_{p,MC}} V_{s,i})$, and 3) find the particle i that has a sum of weight larger than r_2, i.e. $s(i) - r_2 > 0$.

2.2.2. Particle surface discretization

The surface of each individual particle was divided into labeled panels with the same area that can be used to receive droplets.

Table 1
Physical properties of particles and simulation parameters.

Parameter	Value	Unit
Particle phase (HSD and rolling models)		
Particle diameter d_p	1.75 (mono-disperse)	mm
Particle density ρ_p	1420	kg/m^3
Number of particles N_p	50000	–
Coefficient of restitution e	0.69	–
Young's modulus E	10^6	Pa
Poisson ratio σ	0.3	–
Friction coefficient μ_f	0.53	–
Rolling coefficient k_r	0.1	–
Liquid phase (Capillary force)		
Surface tension γ	6.98×10^{-2}	N/m
Contact angle θ	40	°
Parameter $\alpha_l = V_l/(2V_p)$	0.1	%
Gas phase		
Gas density	1.2	kg/m^3
Dynamic viscosity	1.84×10^{-5}	Pa·s
Fluidization gas flow rate $\dot{M}_{g,dry}$	96	kg/s
Atomization gas flow rate	4.2	kg/s
CFD-DEM simulation parameters		
Number of structured CFD cells	81600	–
CFD time step Δt_{CFD}	5×10^{-5}	s
DEM time step Δt_{DEM}	10^{-6}	s
CFD-DEM coupling $\Delta t_{c,1}$	5×10^{-5}	s
CFD-DEM-Monte Carlo coupling $\Delta t_{c,2}$	0.005	s

Supposed that droplets do not overlap, the number of panels per particle N_{dep} was calculated based on the surface area of each primary particle A_p and the mean contact area of single droplet deposition $A_{contact}$; formed as

$$N_{dep,i} = \frac{A_{p,i}}{A_{contact}}, \quad i = 1, \ldots, N_{p,MC}. \tag{2}$$

The calculated number of panels per particle was then rounded to the next integer value. If the shape of deposited droplet is approximated as a truncated spherical cap and the ratio of particle diameter and droplet diameter is large enough, the diameter of contact area is given by (Rioboo et al., 2002; Yarin, 2005)

$$d_{contact} = 2d_d \left[\frac{\sin^3\theta}{2(1-\cos\theta)(2-\cos\theta-\cos^2\theta)}\right]^{1/3}, \tag{3}$$

in which θ is the contact angle between the liquid droplet and the solid particle. For the sake of simplicity, variations of contact angle depending on the surface wettability (Rioboo et al., 2002) in the spreading period were not considered and a constant contact angle was used in the model.

By spherical centroidal Voronoi tessellation (CVT) (Du et al., 1999), a set of N_{dep} points (centroids of panels) can be uniformly distributed on the surface of individual spherical particle. This problem is of great importance in many scientific and engineering applications (Koay, 2011). The main idea of centroidal Voronoi tessellation is that the points used as generators of Voronoi regions coincide with the mass centroids of those regions. In this work, the construction of spherical centroidal Voronoi tessellation was conducted by Lloyd iteration (Lloyd, 1982), as follows:

Step 1: Select a set of N_{dep} points $\boldsymbol{r}_{cvt,i}^{(0)}$ on the surface of a unit sphere based on the standard normal distribution.

Step 2: Construct the Voronoi diagrams associated to the set of points $\boldsymbol{r}_{cvt,i}$, as shown in Fig. 4a). The Voronoi regions V_i of $\mathbb{R}^N$ corresponding to the generators $\boldsymbol{r}_{cvt,i}$ are defined by

$$V_i = \left\{\boldsymbol{x} \in \mathbb{R}^N, \mid \boldsymbol{x} - \boldsymbol{r}_{cvt,i} \mid < \mid \boldsymbol{x} - \boldsymbol{r}_{cvt,j} \mid, j = 1, \ldots, k, j \neq i\right\}, \tag{4}$$

in which $|\cdot|$ denotes the Euclidean norm.

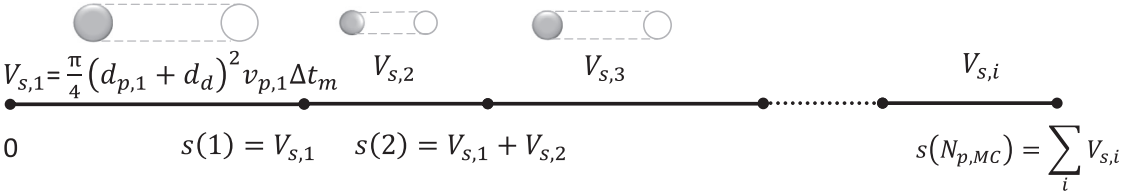

Fig. 3. The weighted random selection of particles based on the volumes swept by the moving particles.

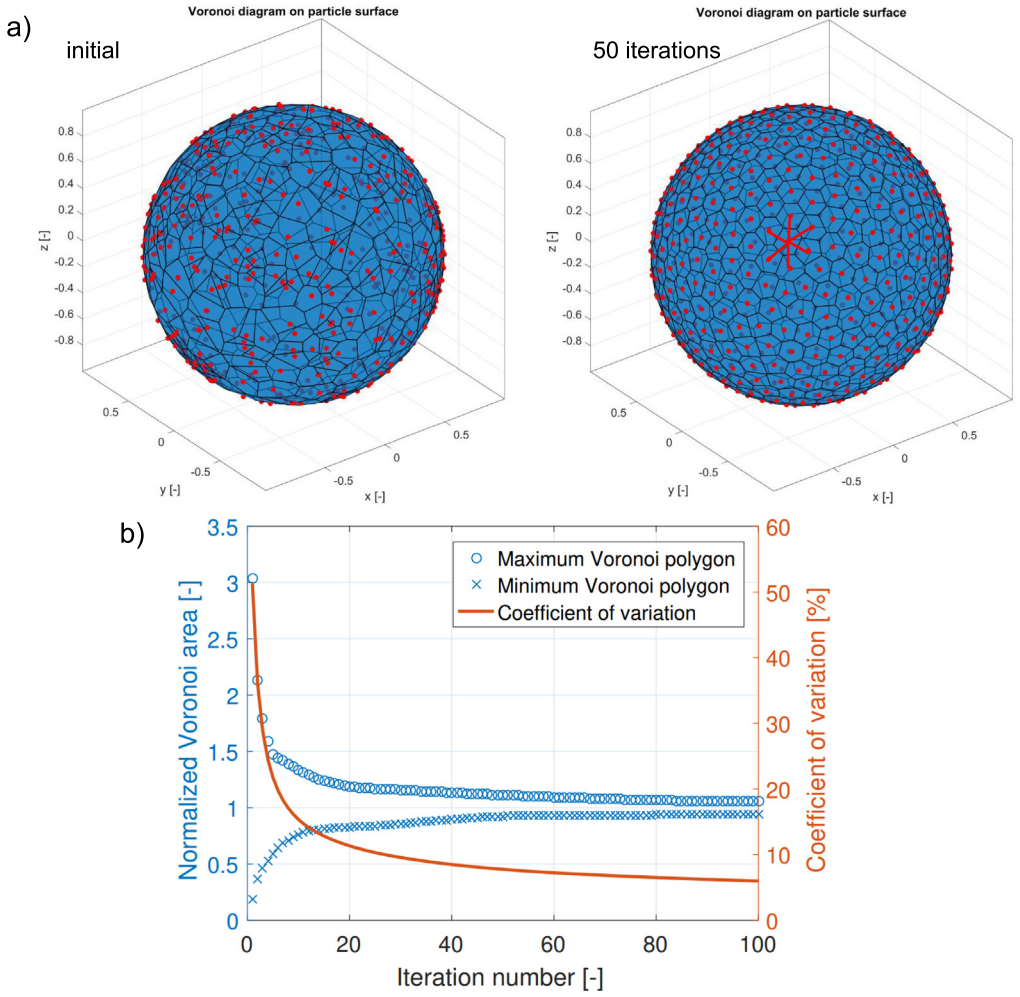

Fig. 4. Centroidal Voronoi tessellation of a spherical particle: a) the set of 500 points (red points) generated via the proposed approach and corresponding Voronoi diagrams (at initial condition and after 50 iteration steps), and b) the normalized maximum and minimum areas of Voronoi tessellations (normalized by $\pi d_{contact}^2/4$) and the coefficient of variation of areas with respect to the number of iterations. The Voronoi first star structure is also depicted using the red lines. (For interpretation of the references to colour in this figure legend, the reader is referred to the web version of this article.)

Step 3: Determine the mass centroids of all Voronoi polygonal regions $\boldsymbol{r}_{cvt,i}^*$. Given a constant probability density function $g(\boldsymbol{x})$ in Voronoi regions V_i, the mass centroids are calculated by

$$\boldsymbol{r}_{cvt,i}^* = \frac{\int_{V_i} g(\boldsymbol{x})d\boldsymbol{x}}{\int_{V_i} \boldsymbol{x}d\boldsymbol{x}}. \tag{5}$$

Then, these centroids $\boldsymbol{r}_{cvt,i}^*$ are used to form the new set of points $\boldsymbol{r}_{cvt,i}$ and the corresponding Voronoi regions V_i.

Step 4: Check the coefficient of variation of areas of Voronoi polygonal regions, as depicted in Fig. 4b). If the Voronoi polygonal regions V_i generated by $\boldsymbol{r}_{cvt,i}$ meets the criterion that the coefficient of variation of areas less than 10%, the iteration terminates; otherwise, return to step 2.

After the spherical centroidal Voronoi tessellation, the centroids of the labeled panels were $\boldsymbol{r}_{cvt,i}$, and the area of every labeled panel is approximately $\pi d_{contact}^2/4$. Fig. 4b) shows that the discrepancy between the normalized maximum and minimum areas of Voronoi tessellations is very small when satisfying the termination criterion. Given that the probability for each panel to get the droplet is the same in this work, a random integer r_3 from the interval $(1,N_{dep})$ can be generated to select the deposition panel for each droplet. Moreover, all information about droplet deposition was stored in the labeled panels on each individual particle.

2.2.3. Droplet deposition

The droplet deposition on each individual panel was affected by both the impact energy of a single droplet and the wetting condition of each individual panel. According to the method used by Jiang et al. (2018a), solid-like droplets with a diameter of 40 μm and a coefficient of restitution of 0.1 were injected in the spray zone of the CFD-DEM simulation to estimate the impact velocity between the particle and the droplet. The computational cost of this simulation is very high due to the required small DEM time step and the large number of particles and solid-like droplets. Based on the results of about 2 s CFD-DEM simulation, the distribution of normal impact velocity v_{rel} between the particle and the droplet was assumed as a normal distribution with a mean of 13.13 m/s and a standard deviation of 3.58m/s in the Monte Carlo model.

The impact of droplets on the dry particle surface exhibits very complex flow patterns, such as deposition, splashing (radial ejecting of secondary droplets due to breakup) and rebounding (partly or fully), which is affected by the droplet size, the impact energy of droplet and the wettability and roughness of the surface (Yarin, 2005; Josserand and Thoroddsen, 2016). The Weber number and Reynolds number characterizing the droplet impact dynamics are

$$We = \frac{\rho_d d_d v_{rel}^2}{\gamma}, \tag{6a}$$

$$Re = \frac{\rho_d d_d v_{rel}}{\mu_d}; \tag{6b}$$

in which ρ_d is the mass density of liquid droplet, γ is the surface tension of droplet, v_{rel} is the normal relative velocity between the particle surface and the droplet, d_d is the diameter of droplet, and μ_d is the dynamic viscosity of droplet. Regardless of surface roughness, the well-known parameter $K_d = We^{1/2}Re^{1/4}$ was used in this work to characterize the transition from deposition to splashing with a threshold value of $K_{d,s} = 57.7$ (Mundo et al., 1995).

If $K_d < K_{d,s}$, the impact was considered to result in normal deposition of the entire volume of the droplet on the deposition panel. If $K_d \geqslant K_{d,s}$, splashing of the droplet occurred. The prompt or corona splashing of suspension droplets on the particle surface and the influence of drying during the impact are very complex. Droplets will break up, redistribute and reshape on the particle surface, and eject small secondary droplets to the surrounding (Josserand and Thoroddsen, 2016). Therefore, the splashing of droplets was regarded as a source of non-uniformity of porosity in the coating layer. In this work, only half of the droplet was assumed to deposit on the considered position, according to the measurement of the number and size distribution of secondary droplets by Yarin and Weiss (1995). The contribution of fine secondary droplets generated by the splashing to the neighboring panels has been neglected.

2.2.4. Droplet drying

A relatively simple drying model was used in this work, in which the drying rate $\dot{m}_{drying}$ (in $\mathrm{kg \cdot m^{-2} \cdot s^{-1}}$) of the first drying period was applied to evaluate the total drying time. The drying rate during the first period is dependent only on the conditions of drying in the Wurster tube, formed as

$$\dot{m}_{drying} = \beta \rho_g (Y_{sat} - Y), \tag{7}$$

in which Y_{sat} is the adiabatic saturation moisture content of the gas, and Y is the moisture content of the bulk gas. Given that, at any time, the amount of evaporated water should be equal to the amount of sprayed water, Y can be calculated by

$$Y = Y_{inlet} + \frac{\dot{M}_l}{\dot{M}_{g,dry}}, \tag{8}$$

in which Y_{inlet} is the moisture content at the inlet, $\dot{M}_l$ is the mass flow rate of the spray liquid, and $\dot{M}_{g,dry}$ is the mass flow rate of the dry fluidization gas. As for a spherical particle, the gas side mass transfer coefficient β can be calculated by the correlation (Gnielinski, 2010):

$$\beta = \frac{Sh \cdot \delta}{d_d}, \tag{9}$$

$$Sh = 2 + \sqrt{Sh_1^2 + Sh_2^2}, \tag{10}$$

$$Sh_1 = 0.664 Re_d^{1/2} Sc^{1/3}, \tag{11}$$

$$Sh_2 = \frac{0.037 Re_d^{0.8} Sc}{1 + 2.443 Re_d^{-0.1}\left(Sc^{2/3} - 1\right)}. \tag{12}$$

Sherwood number Sh represents the ratio of convective mass transfer to the rate of diffusive mass transport and δ is the binary diffusion coefficient of water in air. $Sc = \mu_f/(\rho_g \delta)$ denotes the Schmidt number, and the Reynolds number of the droplet is given by

$$Re_d = \frac{\epsilon_f \rho_f |\boldsymbol{u} - \boldsymbol{v}_i| d_d}{\mu_f}. \tag{13}$$

The magnitude of relative velocity between the gas and the particle that received the droplet $|\boldsymbol{u} - \boldsymbol{v}_i|$ and the volume fraction of gas ϵ_f obtained from the CFD-DEM simulation was used to calculate Re_d.

Then, the drying time Δt_{drying} can be calculated using the drying rate $\dot{m}_{drying}$ and the liquid mass of a single deposited droplet $M_{drop,l}$ to

$$\Delta t_{drying} = \frac{M_{drop,l}}{A_{drop} \cdot \dot{m}_{drying}}, \tag{14}$$

where $A_{drop} = \pi d_{contact}^2/(2 + 2cos\theta)$ is the surface area of the deposited droplet in contact with the gas (Meric and Erbil, 1998). The drying of the liquid droplet was assumed to start after its deposition on the particle at the instant $t_{deposition}$. The following criterion determined if a droplet on the deposition panel had been dried:

$$t_m \geqslant t_{deposition} + \Delta t_{drying}. \tag{15}$$

If the Monte Carlo simulation time t_m was larger than the sum of the deposition time and the drying time of the droplet, the deposition panel was considered dry. In the current model, a droplet can only be deposited on dry or empty panels. Empty panels are either initial panels or new panels generated due to the increase of $d_{p,i}$. If a panel with a wet droplet was selected, a new one was chosen randomly until the surface of selected panel was dry or empty.

2.2.5. Intra-particle coating properties update

According to the method used by Rieck et al. (2016), the layer thickness of the i^{th} individual panel on the j^{th} particle $h_{layer,i,j}$ can be evaluated from the volume of the complete coating layer $V_{layer,i,j}$ assuming every droplet to possess the same solid mass $M_{drop,s,i,j}$. Hence,

$$V_{layer,i,j} = \frac{M_{drop,s,i,j}}{(1 - \epsilon_{layer,i,j})\rho_s} N_{dep,j}, \tag{16}$$

$$h_{layer,i,j} = \left(\frac{d_{core}^3}{8} + \frac{3}{4}\frac{V_{layer,i,j}}{\pi}\right)^{1/3} - \frac{d_{core}}{2}, \tag{17}$$

Table 2
Monte Carlo simulation parameters.

Parameter	Monte Carlo	Experiment
Configuration	Wurster bed	Top-spray bed
Particle material	MCC	γ-Al_2O_3
Coating material	NaB	NaB
Initial bed mass [kg]	0.2	0.4
Initial particle diameter $d_{p,0}$ [mm]	1.75	1.80
Initial particle density [kg/m^3]	1420	1040
Number of particles [–]	50000	125000
Solid density of coating material ρ_s [kg/m^3]	1440	1440
Mass flow rate of solution $\dot{M}_l$ [kg/h]	0.048	0.12
Droplet diameter d_d [μm]	40	40
Viscosity of droplet μ_d [Pa·s]	4.18×10^{-3}	4.18×10^{-3}
Surface tension of droplet γ [N/m]	6.98×10^{-2}	6.98×10^{-2}
Density of droplet ρ_d [kg/m^3]	1125	1125
Contact angle θ [°]	40	40
Solid mass fraction of solution [%]	30	30
Porosity of the coating layer [%]	30	30
Inlet temperature of gas [°C]	75	75
Inlet moisture content of gas Y_{inlet} [g/kg]	1	1
Mass flow rate of gas $\dot{M}_{g,dry}$ [kg/h]	96	120

where d_{core} is the diameter of the core particle. In the current work, the porosity of layer $\epsilon_{layer,i,j}$ for normal deposition was a constant model parameter according to the X-ray micro-computed tomography experiments ($\epsilon_{layer,i,j} = 0.3$, Table 2, Sondej et al. (2015)). Splashing is not considered to affect layer thickness; instead, layer porosity increases compared with normal droplet deposition. Keeping the factor $M_{drop,s,i,j}/(1-\epsilon_{layer,i,j})$ constant for both, normal and splashing deposition results in a higher porosity of $\epsilon^*_{layer,i,j} = 0.65$ for splashing deposition.

Moreover, the average layer thickness (intra-particle) and the diameter of each particle can be written as:

$$h_{m,j} = \frac{1}{N_{dep,j}}\left(\sum_i^{N_{dep,j}} h_{layer,i,j}\right), \tag{18}$$

$$d_{p,j} = d_{core} + 2h_{m,j}. \tag{19}$$

The diameter of each particle was given back to the DEM solver. The mean layer thickness in the particle population (inter-particle) was calculated by

$$h_m = \frac{1}{N_p}\left(\sum_j^{N_p} h_{m,j}\right). \tag{20}$$

To evaluate the coating coverage of each particle, the number of initial deposition panels $N_{dep,j}$ and the number of deposition panels that have received droplets (dry or wet) $N_{coat,j}$ were counted. Then, the following equation was used to calculate the coating coverage of each particle Ψ_j in each time step:

$$\Psi_j = \frac{N_{coat,j}}{N_{dep,j}}. \tag{21}$$

If the coating coverage of the particle reaches 100%, a full closed coating layer has formed around the particle. The average inter-particle coating coverage is

$$\Psi_m = \frac{1}{N_p}\left(\sum_j^{N_p} \Psi_j\right). \tag{22}$$

2.3. Simulation setup

2.3.1. CFD-DEM

In this work, the geometry of the Wurster coater was built according to the positron emission particle tracking (PEPT) measurements of Li et al. (2015a); and the operation condition was set according to the run number 16 in their measurements. The total batch mass of 1.75 mm microcrystalline cellulose (MCC) particles is 200 g (about 50000 particles). The diameter and length of the concentric cylindrical Wurster tube are 50 mm and 150 mm, respectively. There is a 15 mm partition gap between tube bottom and the distributor plate. A circular symmetric spray zone with inflection boundaries (Börner et al., 2014) was predefined in the CFD-DEM simulation, in which the maximum penetration starting from the nozzle tip is 75 mm and the spray angle is about 52.5° (as shown in Fig. 1). The volumes of the spray zone and the Wurster tube are 0.19×10^{-3} and 1.18×10^{-3} m^3, respectively. In total, 81600 hexahedral grids were built using the orthogonal grid method. The details about bed dimensions, structured grids, boundary conditions and mesh independence can be found in our previous published work (Jiang et al., 2018a).

Detailed material properties of MCC particles related to the HSD, the rolling and the capillary force models are given in Table 1. The coefficient of restitution e was directly measured by the free fall test using a vibratory feeder and a high-speed imaging system as presented in Jiang et al. (2019). Youngs modulus E and the friction coefficient μ_f were taken from Li et al. (2015b). The Poisson ratio σ was measured by Roberts et al. (1994). Similar to the method of Goniva et al. (2012), the rolling coefficient k_r in the directional constant rolling friction model was calibrated based on the static angle of repose of MCC particles.

Time step should be smaller than some critical value to conform with physical laws and guarantee stability in DEM and CFD solvers. The CFD time step was set to 5×10^{-5} s, which ensured that the maximum Courant number was less than 0.5 (for stability). The collision time τ_H can be estimated based on HSD contact theory (Antypov and Elliott, 2011):

$$\tau_H = 2.21\left(\frac{\rho_p}{E_{eq}}\right)^{2/5}\frac{d_p}{v_{c,max}^{1/5}}. \tag{23}$$

Assuming a maximum collision velocity $v_{c,max}$ of 1.5 m/s in the whole bed (Jiang et al., 2017), the estimated collision time τ_H for two 1.75 mm particles is approximate 2.6×10^{-5} s. Hence, the DEM time step was set as 10^{-6} s, less than $\tau_H/20$ of particles, to ensure the accuracy of HSD contact model. The coupling interval between the DEM and CFD solvers $t_{c,1}$ was set to 50 times the DEM time step, i.e. 50 µs.

CFD-DEM simulations of two cases were performed using four-way coupling by the code OpenFOAM and LIGGGHTS (Goniva et al., 2012). The first case without capillary forces between particles can be directly compared to the PEPT measurement at dry condition by Li et al. (2015a). The second case with capillary forces was designed to investigate the influence of wetting and agglomeration in the Wurster tube on the residence time distribution. The liquid bridges were assumed to be formed by sodium benzoate (NaB) solution with a mass fraction of approximately 30%. The surface tension of the liquid γ was measured by the pendant drop method (Table 1). As measured by Zhu et al. (2013), the motion of particles in spouted beds was significantly influenced by the effects of cohesion as α_l exceeded 10^{-3}. Therefore, the parameter α_l was set as 0.1% in order to investigate the effects of cohesion on particle circulation. In other words, the parameter α_l was purposely enlarged, compared with the value of 6×10^{-6} calculated by the volume of a single droplet used in the Monte Carlo (Table 2).

2.3.2. Monte-Carlo

A relatively large $t_{c,2} = 0.005$ s, about 1/200 of the mean residence time in the tube and 1/30 of the mean residence time in the spray zone, was used to avoid excessively high computational

cost because of too frequent communication between CFD-DEM code and Monte Carlo method.

Sondej et al. (2015, 2016) measured both the intra-particle and inter-particle distributions of coating layer thickness in a top-spray fluidized bed. In their experiment series A, the diameter of the core particles was 1.8 mm which is similar to the value of 1.75 mm used in the current simulations. In order to compare with their experiment, the mass flow rate of spray solution $\dot{M}_l$ used in the Monte Carlo model was scaled according to the numbers of primary particles in the different beds, which leads to similar values of the mean layer thickness and mean coating mass per particle. Although the coating performances of the top-spray fluidized bed and the Wurster fluidized bed are not exactly the same, the comparison of intra-particle layer thickness distribution is still meaningful when the mean coating mass received by individual particles is the same. The coating material is sodium benzoate, which has an antibacterial effect and is used as a preservative in the food industry. The mass fraction of sodium benzoate solution is about 30%. The viscosity of the solution was measured by a Hppler viscosimeter; and the density of the liquid was measured by a density meter (DMA 58, Anton Paar). Other properties associated with the spray droplets and gas flow were set same as in the corresponding experiment series A (Sondej et al., 2016). Detailed parameters of the Monte Carlo model and the experiment are listed in Table 2.

2.4. Recurrence of particle circulation

In this work, the CFD-DEM takes about 5 h to simulate 1 s real time (with 8 CPUs), while the Monte Carlo only needs about 0.05 h. If the simulation had to be performed, for example, 1 h to predict a real coating process, it would take more than 750 days, which is not acceptable.

In the CFD-DEM-Monte Carlo model, the coating of particles is largely determined by the cycle time distribution and residence time distribution in the spray zone obtained from the CFD-DEM, with the details of droplets deposition, drying and solidifying being modeled by the Monte Carlo. It was found that the distributions of cycle time and residence times are almost constant after 60 s. As listed in Table 3, the deviations of mean cycle time, mean ideal cycle time, mean residence times in the tube and the spray zone, as well as the corresponding coefficients of variation are very small between 60 s and 180 s. Based on the circulation characteristics of particles, it is thus reasonable to use the database of particle dynamics obtained from a relative short duration to reconstruct the recurring motion of particles in a long-term period. In this work, a simple approach was used to recur the particle circulation motion, as follows:

First, the database of 50000 individual particles was generated using the full CFD-DEM-Monte Carlo simulation data in the duration of 180 s, including particle positions $\boldsymbol{r}_i$, particle velocities $\boldsymbol{v}_{p,i}$, relative velocities between particles and the fluid phase $\boldsymbol{u} - \boldsymbol{v}_{p,i}$, particle diameter $d_{p,i}$ and the indicator $I_{A_c,i}$. Based on the trajectory of each individual particle, the indicator function was defined to indicate the occurrence of event A_c that the particle entered into the spray zone through the partition gap at instant t, expressed as

$$I_{A_c}(t) = \begin{cases} 1, & if\ t \in A_c, \\ 0, & if\ t \notin A_c. \end{cases} \tag{24}$$

In other words, the instant t corresponds to the start point of a new cycle as $I_{A_c}(t) = 1$.

Second, for each individual particle, the particle dynamics after the last instant t satisfying $I_{A_c,i}(t) = 1$ in the full simulation can be recurred by repeatedly extrapolating the particle dynamics in the range of $(t_{r,j}, t_{r,j+1}]$ from the database. The instant $t_{r,j}$ was a randomly selected instant that corresponds to $I_{A_c}(t_{r,j}) = 1$; and $t_{r,j+1}$ was the next instant that made the indicator function equal to unity. As listed in Table 3, the relative deviations of mean cycle time, mean ideal cycle time, mean residence times in the tube and the spray zone as well as the corresponding coefficients of variation are all almost negligible (less than 1%) between the full simulation results of 180 s and recurring results of 1 h by this method.

It is emphasized that this simple approach to recur the particle circulation only reproduces the circulating motion. However, if the database obtained from the full simulations is large enough, this simple method is statistically reliable and can well predict the distributions of cycle time and residence times in the Wurster fluidized bed with negligible computation cost compared with the CFD-DEM. Therefore, the CFD-DEM simulation was terminated after 180 s in this work; subsequently, the particle dynamics required in the Monte-Carlo model were extrapolated from the database. The total computational times of CFD-DEM and Monte Carlo to model one-hour coating process were about 900 h and 180 h, respectively. Additional 20 h were used to repeatedly

Table 3
Comparison of ideal cycle time, overall cycle time, and residence times in the Wurster tube and the spray zone obtained from CFD-DEM simulations for dry conditions as well as with cohesion forces ($\alpha_l = 0.1\%$); and the PEPT measurement (Li et al., 2015a).

Variable	CFD-DEM simulations					PEPT
	dry (10 s)	dry (60 s)	dry (180 s)	dry (1 h)	$\alpha_l = 0.1\%$ (1 h)	dry (1 h)
$\bar{t}_{ic}$ [s]	4.76	4.97	4.98	4.98	4.75	4.84
$C_v(t_{ic})$ [%]	68.7	53.3	52.5	52.8	43.5	99.0
$\bar{t}_c$ [s]	5.63	5.80	5.83	5.82	6.02	6.14
$C_v(t_c)$ [%]	88.3	61.4	62.0	61.5	70.3	90.0
$\bar{t}_{r,t}$ [s]	0.891	0.958	0.965	0.963	0.925	1.00
$C_v(t_{r,t})$ [%]	51.6	33.0	34.3	33.7	54.6	–
$\bar{t}_{r,s}$ [s]	0.136	0.156	0.158	0.158	0.153	–
$C_v(t_{r,s})$ [%]	47.8	23.7	22.5	22.1	42.3	–
R_{ic} [%]	69.3	77.3	78.4	78.3	60.2	55.3

[1] $\bar{t}_{ic} = \sum_j^{N_{ic}} t_{ic,j}/N_{ic}, N_{ic}$ is total number of ideal cycles, $t_{ic,j}$ is time of each ideal cycle.

[2] $\bar{t}_c = \sum_j^{N_c} t_{c,j}/N_c, N_c$ is total number of cycles, $t_{ic,j}$ is time of each cycle.

[3] $\bar{t}_{r,t} = \sum_j^{N_c} t_{r,t,j}/N_c, t_{r,t,j}$ is residence time in the Wurster tube in each cycle.

[4] $\bar{t}_{r,s} = \sum_j^{N_c} t_{r,s,j}/N_c, t_{r,s,j}$ is residence time in the spray zone in each cycle.

[5] $R_{ic} = N_{ic}/N_c$.

[6] C_v is the coefficient of variation.

extrapolate the particle dynamics. It should be noted that the influence of increasing particle diameter $d_{p,i}$ on the particle dynamics cannot be captured in this way. However, this influence is very limited for particles with very thin coating layers considered in this work.

3. Results and discussion

The results obtained from the coupled CFD-DEM-Monte Carlo method will be presented in form of the residence and cycle time distributions, and the intra-particle and inter-particle coating properties. Residence and cycle time distributions are compared with PEPT measurement data (Li et al., 2015a); and the intra-particle coating layer thickness distribution is compared with experimental data gained by X-ray micro-computed tomography (μ-CT) (Sondej et al., 2015; Sondej et al., 2016).

3.1. Residence and cycle time distributions

The particle oriented features of the CFD-DEM simulation environment were advantageous to investigate the circulation of particles in the Wurster fluidized bed. As depicted in Fig. 1, the chamber of the Wurster fluidized bed is divided into: (1) spray zone, (2) Wurster tube (without overlap with the spray zone), (3) fountain zone (only a part of the fountain zone is depicted for better visualization), (4) down bed, and (5) horizontal zone. In each ideal cycle, particles move upward into the tube from the spray zone, lose momentum in the fountain zone, fall down into the external annulus, are transported in the horizontal zone in plug flow manner, and re-enter the spray zone through the partition gap at the bottom of the internal annulus. Particles can recirculate within the Wurster tube without passing the partition gap, including the motion from zone 2 to zone 1 and from zone 3 to zone 2. The recirculation influences the distributions of cycle time and residence time in the spray zone and Wurster tube. In this work, the ideal cycle and nonideal cycle were distinguished by the determination of the appearance of recirulation based on particle trajectories (Jiang et al., 2018a). The cycle time of particles related to the number of passes through the spray zone and the residence time in the spray zone related to the amount of the obtained coating material per cycle are two significant parameters for the uniformity of the coating process.

Simulation results associated with distributions at different processing times are summarized in Table 3. Data for 10 s, 60 s and 180 s come from the full simulations, and data for 1 h was evaluated based on the recurrence of particle circulation, as discussed in Section 2.4. Comparing the data of 180 s and 1 h for dry condition without capillary forces in the DEM shows that the recurrence method well reconstructs the long-term circulation of particles in terms of mean values of cycle time t_c, ideal cycle time t_{ic}, residence time in the spray zone $t_{r,s}$ and residence time in the Wurster tube $t_{r,t}$ as well as the corresponding coefficients of variation. However, if the database is not big enough for the recurrence process (for instance after only 10 s), large deviations will be introduced into the recurring data and final coating properties. To apply the recurrence method for the Wurster fluidized bed, the full CFD-DEM simulation must be performed at least until stabilization of the mean cycle time of particles has been achieved.

Comparing the data of simulation for dry condition with the PEPT measurement (Li et al., 2015a), the mean of ideal cycle time obtained from the simulation is found to be slightly higher; inversely, the mean of total cycle time is under-predicted, which is due largely to a high fraction of ideal cycles in the simulation. In the simulation, most of the non-ideal cycles were caused by intensive interactions with the Wurster tube wall and other particles. Further discussion on the possible reasons would require more information about particle–particle and particle–wall interactions from the PEPT measurements. Moreover, the distributions of total cycle time and ideal cycle time were found to be fairly broad for the PEPT measurement, the spreads predicted by the simulation being somewhat smaller. These observations are similar to those made on simulations for binary particle mixtures (Jiang et al., 2018a). The mean residence times in the Wurster tube were found to be in good agreement with experimental data. The mean residence time in the spray zone is 0.158 s (about 1/6 $\bar{t}_{r,t}$) based on the geometry of the predefined spray zone. Note that only a single tracer particle was used in PEPT measurement. According to the concept of ergodicity, the distribution of circulations was evaluated by the motion of this tracer particle in a long tracking period of about 1 h.

Additionally, the influence of capillary forces in the Wurster tube on the circulation motion was investigated by the cohesion DEM model. Fig. 5 shows snapshots of particle motion for conditions with and without capillary force. The global circulation of particles with capillary forces ($\alpha_l = 0.1\%$) is very similar to that at dry condition; however, the particles tend to be agglomerated by the liquid bridges as the inter-particle distances are shorter than the rupture distance. Because no drying and solidification of liquid bridges were considered in CFD-DEM simulations, the agglomerates formed by liquid bridges were not stable, and could break up as the relative distances between particles in the agglomerates varied due to collisions with the tube wall or other particles (or agglomerates). Comparing the simulation results of the two cases in Table 3, the capillary force decreases the mean ideal cycle time

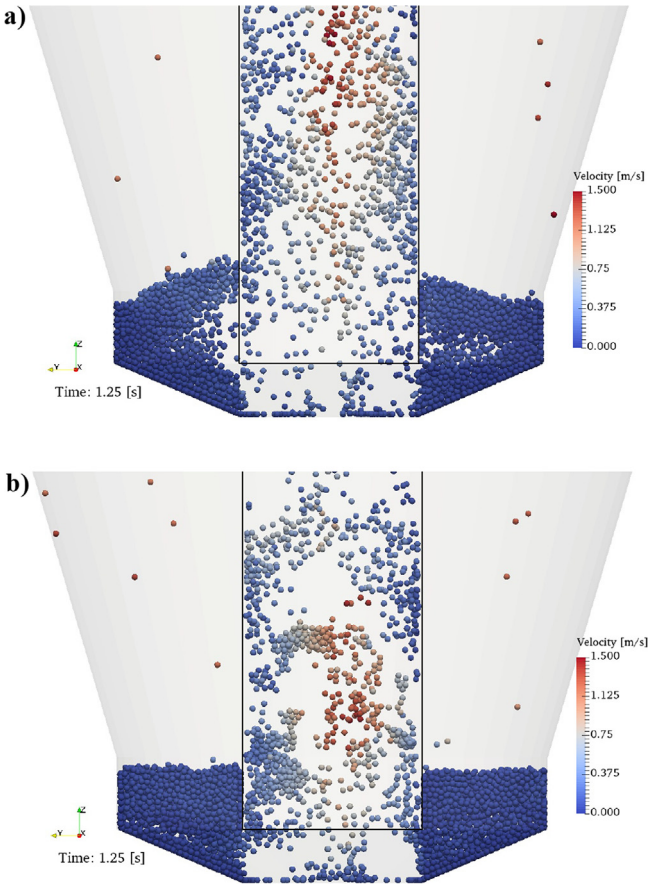

Fig. 5. Snapshot of particle motion in the Wurster fluidized bed: a) without cohesion force, b) with cohesion force ($\alpha_l = 0.1\%$).

as well as the mean residence times in the Wurster tube and in the spray zone. Since agglomeration of particles increased the local solid volume fractions ϵ_s in Eq. (A.7), momentum exchange between particles and the gas in these regions and the mean velocities in vertical direction in the Wurster tube were increased. Nevertheless, the capillary force decreases the fraction of ideal cycles R_{ic} due to more complex interactions between temporary agglomerates and the tube wall. As a consequence of this decrease, the capillary force further scatters the distributions of total cycle time, and residence times in the Wurster tube and the spray zone. This effect is more obvious in the Wurster tube. It is therefore important to provide enough drying capacity of the fluidization gas, so that particles are dry before re-entering the spray zone. The influence of the capillary force is expected to be more pronounced in coating of fine particles, and is subject of further investigations.

3.2. Morphology of coating layer

3.2.1. Coating properties of a sample particle

Fig. 6 illustrates the coating properties of a random sample particle predicted by the simulation without capillary forces. The intra-particle coating coverage is an important property for functional coatings especially in pharmaceutical film coating applications. The variations of coating coverage from 20 s to 100 s are shown in Fig. 6a). Droplets on the deposition panels can be dried (gray color) or wet (blue color) depending on Eq. (15). The coating coverage Ψ increases from 9.24% to 33.51% in a duration of 80 s, which is affected by both the cycle time and residence time of this particle in the spray zone.

At process times of 500 s, 1500 s and 3000 s, the coating layer thickness and the splashing positions along a great-circle of the

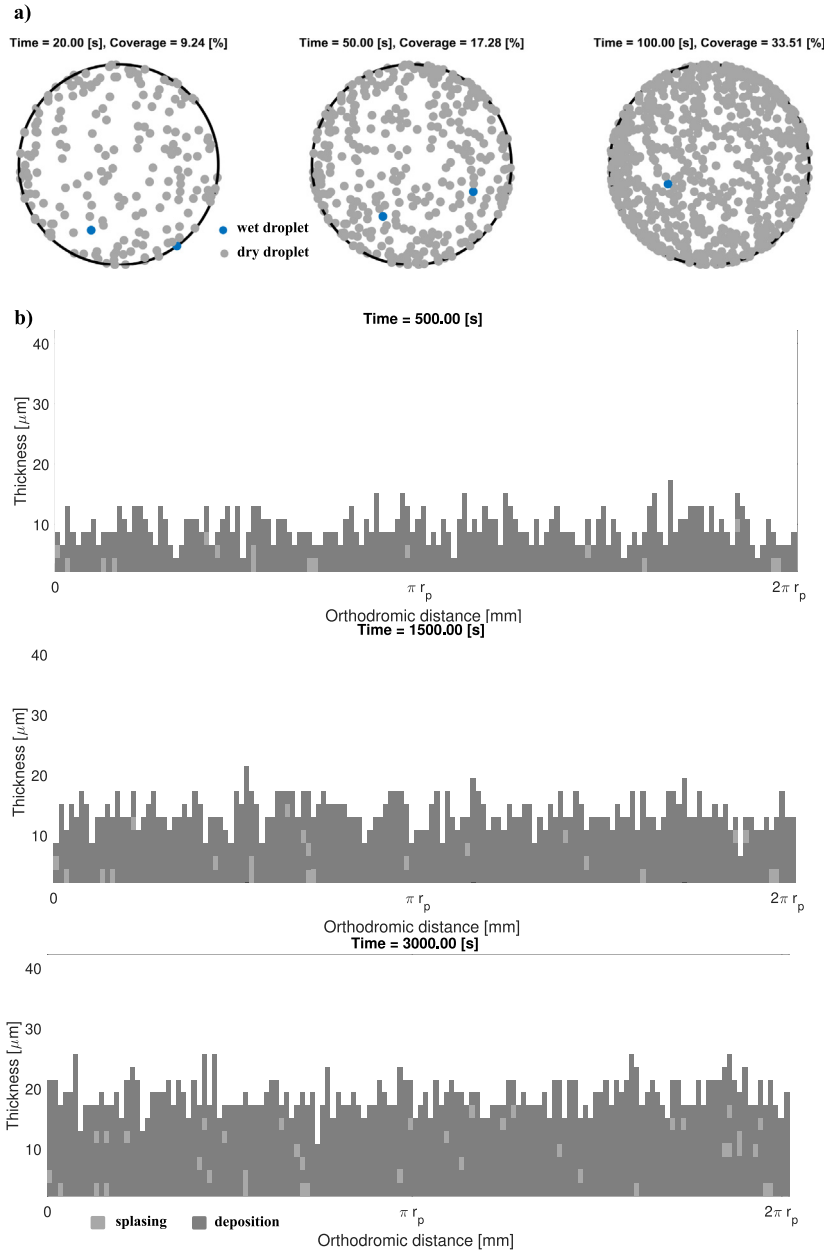

Fig. 6. Coating quality of single sample particle: a) coating coverage (2D front elevation), b) coating layer thicknesses and splashing positions along a great-circle of the spherical particle.

spherical particle are depicted in Fig. 6b). The layer thickness on each panel on the single particle was calculated by Eq. (17). The information on layer thickness of each panel can be further used to evaluate the uniformity of coating by, for instance, the mean layer thickness $h_{m,j}$ (Eq. (18)), the standard deviation, the coefficient of variation and the arithmetic average roughness.

In the current Monte-Carlo model, the porosity of splashing panels was assumed to increase, due to lower volume of received droplet, changes in droplet shapes, as well as droplet drying and solidification during the impact. The splashing panel is drawn with a relatively light color, which implies a relatively high porosity. For an individual splashing position, the orthodromic distance to its nearest neighboring splashing position on the same layer was defined as L_{min}, which can be further normalized by the particle radius r_p. For the sample particle at 3000 s, the mean and the coefficient of variation of L_{min}/r_p are 0.224 and 45.2% in the 3D space, respectively. In addition, the size of individual high porosity regions S_p was defined by the number of connected splashing positions. If several splashing positions with the same radial distance belonged to the same Voronoi star, these positions were considered as a connected high porosity region at this radial distance. The Voronoi star was assembled by the centroid (the center of star) and corresponding natural neighboring points (endpoints of the extremities of the star) in the Voronoi diagram (Jiang et al., 2017), as shown in Fig. 4. If several high porosity regions at different radial distances were overlapping, these high porosity regions were merged. For the sample particle at 3000 s, the mean and the coefficient of variation of S_p are 1.21 and 42.8% in the 3D space, respectively. Usually, the risk to form cracks and large pores in the coating layer increases with decreasing L_{min} and increasing S_p.

At 500 s, all deposition panels along the chosen great-circle have been coated. However, this does not imply complete coating in all great-circles. Actually, the time to accomplish the 100% coating coverage $t_{cover,100}$ for this sample particle is about 880 s.

3.2.2. Layer thickness

Fig. 7 shows intra-particle cumulative distributions of coating layer thickness. The individual particles correspond to 0.1, 0.5, and 0.9 of the property value in the population. Besides the plotted distributions, the mean values and coefficients of variation of intra-particle and inter-particle coating properties are listed in Table 4 to further characterize the distributions.

It can be seen that the predicted results of MC-50 for both conditions are close to the measurement data. The distance between the curves of MC-10 and MC-90 for the condition with capillary forces is much larger than that for simulation without capillary forces, corresponding to a wider distribution of residence time in the spray zone with comparable mean value (Table 3). Compared with the Monte Carlo modeling of Rieck et al. (2016) (Exp. 3), the deviations of mean layer thickness between different single particles are much larger, as a result of the non-uniformity of residence times and cycle time predicted by the CFD-DEM. However, the coefficients of variation of all single particles for both conditions are very close, since the probability for each panel to receive droplets was similar and only affected by the number N_{dep} in the Monte-Carlo model. If layer thickness of the particle is 30 μm, then there will be about 6.9% increase in N_{dep} due to growth of a 1.75 mm core particle.

In addition to the intra-particle scale, the distribution of mean layer thickness per single particle in the population (inter-particle) can also be extracted from the simulations (Table 4). It is interesting to observe that the coefficient of layer thickness variation in the particle population is much smaller than the values for the single particles (Table 4). The predicted value of 7.7% is comparable to the value of 5.1% for the particle population in the experimental data for top-spray coating of Sondej et al. (2015). Information about the RTDs in the coupled CFD-DEM-Monte Carlo approach can better represent the situation in experimental equipment under different operation conditions than the spatially concentrated, single compartment Monte Carlo approach by Rieck et al. (2016).

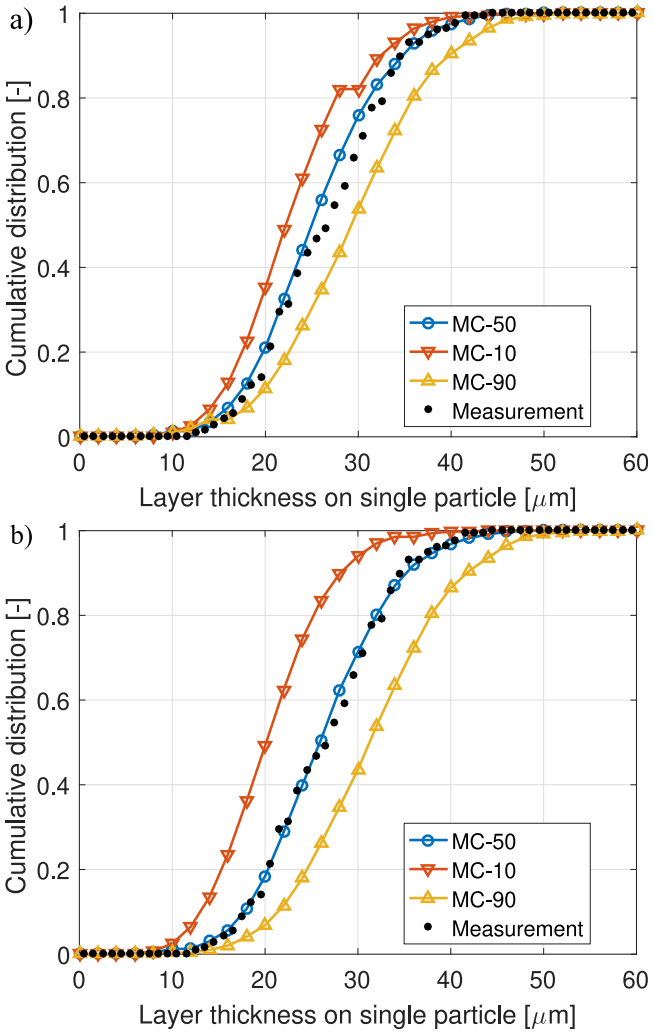

Fig. 7. Comparison of cumulative distributions of layer thickness on single particles obtained from the measurement and the CFD-DEM-Monte Carlo simulations at 1 h processing time: a) without cohesion force, and b) with cohesion force ($\alpha_l = 0.1\%$).

3.2.3. Coefficient of variation of coating layer thickness

When the same amount of material is deposited on each particle for each pass through the spray zone, the coefficient of variation of the inter-particle coating mass distribution is given by (Cheng and Turton, 2000)

$$C_{v,inter,m} = C_v(t_c)\sqrt{\frac{\bar{t}_c}{t_{coat}}}, \tag{25}$$

in which $C_v(t_c)$ is the coefficient of variation of cycle time (Table 3), $\bar{t}_c$ is the mean cycle time and t_{coat} is the total coating time. The coefficient of variation of the intra-particle layer thickness is proportional to the number of coating passes raised to the $-1/2$ power (Freireich and Wassgren, 2010). When every deposition panel has

Table 4
Summary of intra-particle (10%, 50%, 90%) and inter-particle coating properties obtained from simulations without and with capillary force.

Coating properties	Simulation without cohesion				Simulation with cohesion $\alpha_l = 0.1\%$			
	10%	50%	90%	inter	10%	50%	90%	inter
$mean(h)$ [μm]	24.28	26.17	29.86	26.03	21.75	26.94	32.25	26.77
$C_v(h)$ [%]	26.8	27.0	27.1	7.7	27.3	26.5	26.0	12.4
$mean(S_p)$ [%]	1.13	1.34	1.58	1.36	1.13	1.36	1.62	1.39
$C_v(S_p)$ [%]	20.7	32.3	44.7	6.9	22.8	34.1	46.0	7.7
$mean(L_{min}/r_p)$ [–]	0.177	0.206	0.248	0.215	0.173	0.209	0.261	0.219
$C_v(L_{min}/r_p)$ [%]	40.7	47.4	55.7	12.9	41.0	47.3	54.6	15.5
$mean(t_{cover,100})$ [s]	898	1213	1621	1245	882	1284	1997	1258
$C_v(t_{cover,100})$ [%]	–	–	–	22.7	–	–	–	27.5

an equal opportunity of being coated and only one deposition panel can receive the droplet in each Monte Carlo time step, Eq. 28 in Freireich and Wassgren (2010) can be rewritten as

$$C_{v,intra,l} = \sqrt{\frac{1}{N_{drop}}\left[N_{dep} + (N_{drop} - 1)\right]} - 1, \tag{26}$$

where N_{drop} is the number of droplets deposited on the certain particle.

According to simulation data, the coefficients of variation of intra-particle and inter-particle layer thickness distribution can be directly calculated based on Eq. (17) and Eq. (18), respectively. Fig. 8 depicts the coefficients of variation from the simulation without capillary forces and from analytic models as functions of coating time. It can be seen that the coefficients of variation of intra-particle coating layer thickness predicted by the simulation (MC-10, MC-50 and MC-90) almost coincide with that of the analytic model after about 1500 s. In the simulation, the amount of material that is deposited on each particle in each pass is affected by the volume swept by the moving particle and residence time in the spray zone. As a result, the inter-particle coefficient of the coating mass distribution predicted by the simulation is larger than that of the analytic model. The inter-particle coefficient of the coating mass distribution predicted by the simulation is very similar to that of the coating layer thickness. However, the difference between the two curves gradually becomes distinct, since the distribution of N_{dep} spreads with increasing coating time. Generally, the trend is that the coefficient of variation quickly decreases in the initial stage and then it gradually asymptotes to zero as time increases. The reduction of the value of the coefficient of variation on the inter-particle scale is faster than that on the intra-particle scale.

3.2.4. Coating coverage and uniformity

Fig. 9 shows the changes of mean coating coverage Ψ_m of all individual particles with coating time. It takes more than 1600 s to achieve a completely closed coating layer on every individual particle in both simulation cases. The rate of increase of coating coverage incrementally decreases as the coating time increases. The mean coating coverage of the simulation without capillary forces is slightly larger than that of the simulation with capillary

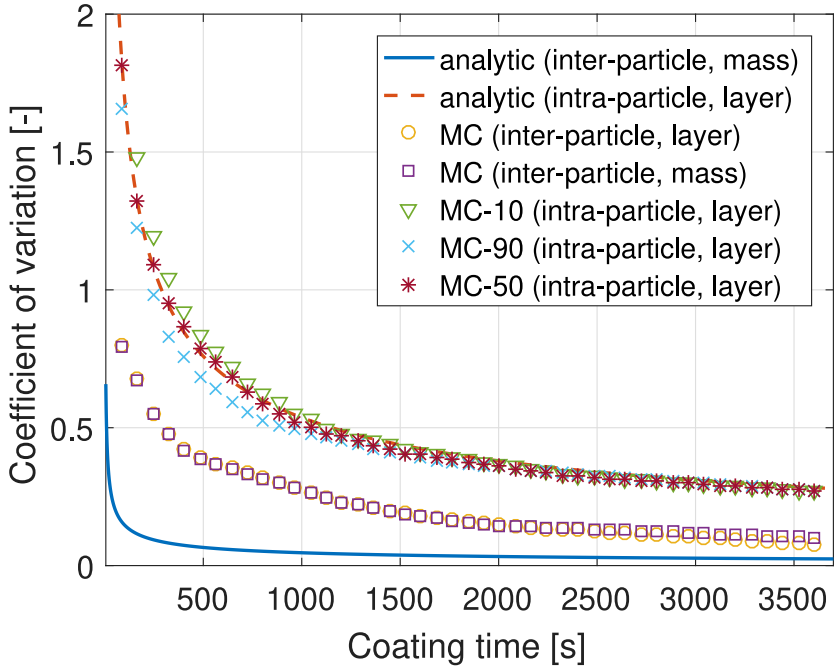

Fig. 8. Comparison of the coefficients of variation of inter-particle and intra-particle layer thickness distributions obtained from the simulation without capillary forces, inter-particle analytic model of coating mass distribution (Cheng and Turton, 2000), and intra-particle analytic model of layer thickness distribution (Freireich and Wassgren, 2010).

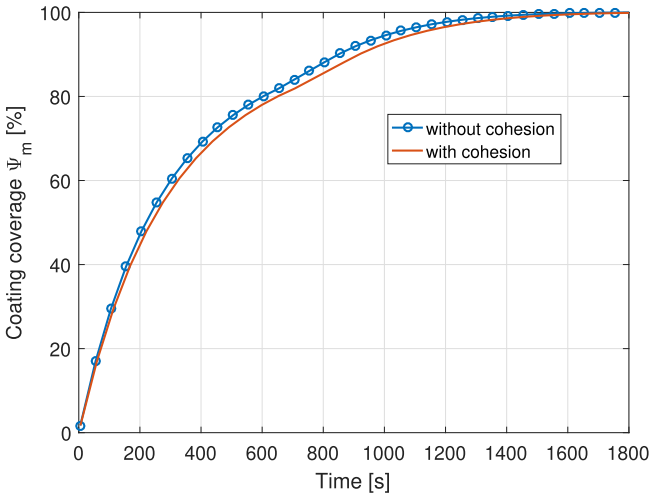

Fig. 9. Mean coating coverage Ψ_m obtained from simulations with ($\alpha_l = 0.1\%$) and without capillary forces with respect to coating time.

forces, which can be traced back to the influence of the capillary force on the RTDs in the Wurster coater. Fig. 10 shows the density distributions of coating coverage Ψ_j obtained from the simulation without capillary forces for different processing times. The coating coverage can be seen to experience a highly peaked distribution at 50 s, flat distributions at 100 s and 200 s, and a highly skewed distribution towards 100% at 500 s. Note that 100% is the maximum value that can be achieved according to Eq. (21). The shape of the distribution of coating coverage was mainly affected by the RTDs in the bed. It is found that the distributions of coating coverage closely follow the Weibull distribution

$$f_w(x) = \begin{cases} \frac{k_1}{k_2}\left(\frac{x}{k_2}\right)^{k_1-1} e^{-(x/k_2)^{k_1}}, & x \geqslant 0, \\ 0, & x < 0. \end{cases} \tag{27}$$

The shape parameter k_1 and scale parameter k_2 are used to fit the simulation data given in Fig. 10. Furthermore, information about the time to achieve 100% coverage is also listed in Table 4. The difference of $t_{cover,100}$ at 90% of the cumulative distribution with and without capillary force is longer than 6 min, due to the wider RTDs predicted by the simulation with capillary forces.

Fig. 11 shows the cumulative distributions of L_{min}/r_p and S_p for the particle population. When capillary force is taken into account in the DEM, the spreads of distributions of L_{min}/r_p and S_p slightly increase due to the effect on RTDs. According to the related data listed in Table 4, the coefficients of variation are again much smaller than the values obtained for the single particles.

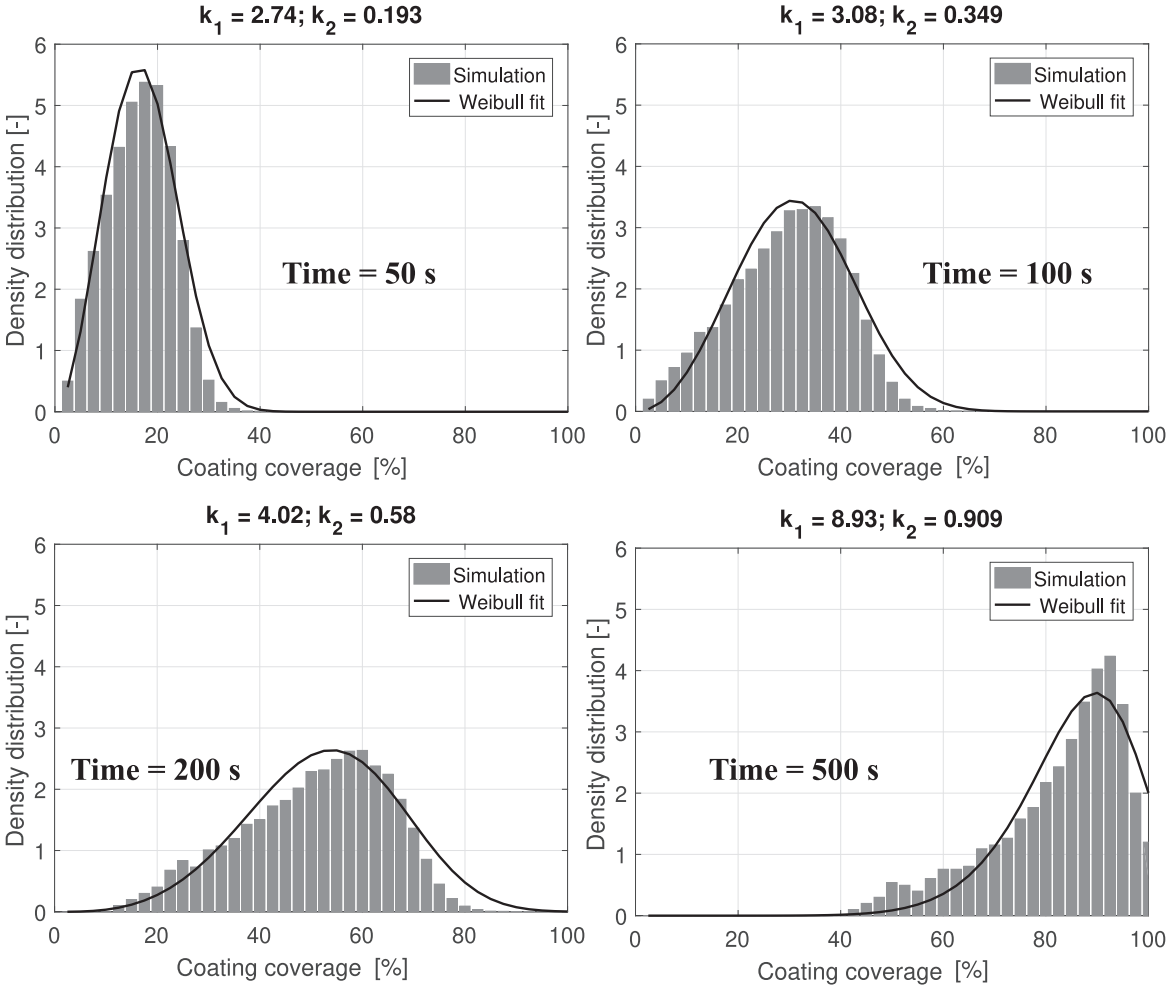

Fig. 10. Simulation results (without capillary forces) of probability density distributions for coating coverage (grey histograms) of all individual particles at 50 s, 100 s, 200 s and 500 s, together with the fitted Weibull distributions (black lines).

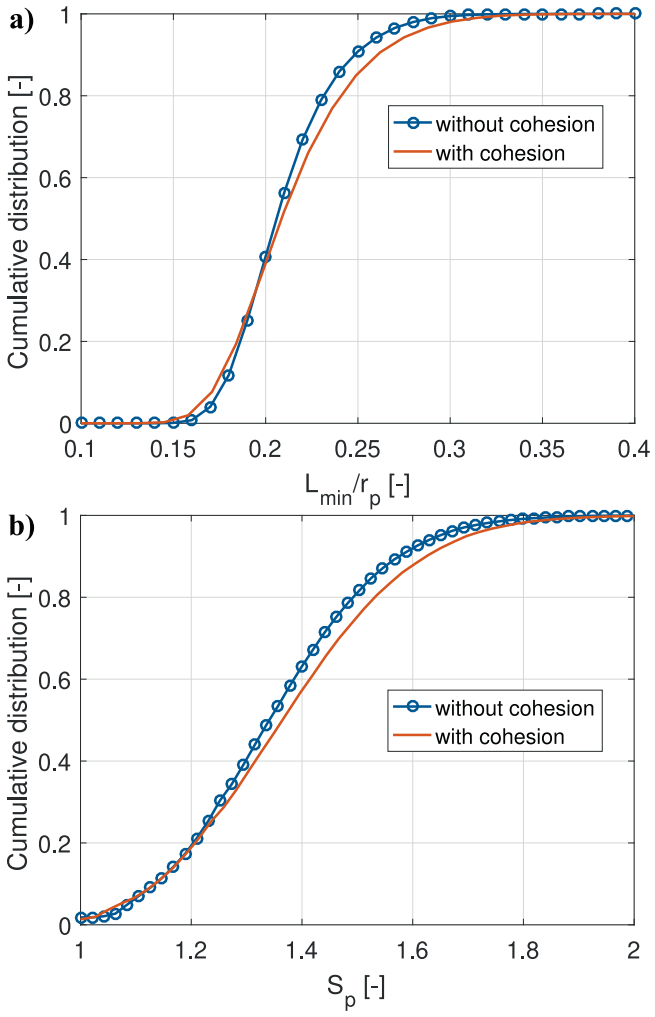

Fig. 11. Cumulative distributions of inter-particle properties associated with high porosity regions induced by droplet splashing: a) L_{min}/r_p, and b) S_p ($\alpha_l = 0.1\%$ in the capillary force model).

4. Conclusion and outlook

This work presented a combined methodology for simulating particle dynamics as well as the inter-particle and intra-particle morphology of coating layers using a coupled CFD-DEM-Monte Carlo approach. The circulation motion of particles in the Wurster fluidized bed was predicted by the CFD-DEM approach for conditions with and without capillary forces induced by liquid bridges. The deposition, splashing, and drying of droplets on the individual particle surface were described by the Monte Carlo approach together with the spherical centroidal Voronoi tessellation (CVT).

The RTDs in the Wurster fluidized bed predicted by CFD-DEM simulations without capillary forces were found to be in good agreement with PEPT measurement results. However, the fraction of non-ideal cycles was underestimated in the simulation, which may be caused by particleparticle and particlewall interactions in the Wurster tube. When the capillary force induced by liquid bridges between particles is included in the DEM, the spread of the RTDs in the spray zone and in the Wurster tube increases significantly. According to the circulation features in the Wurster fluidized bed, the cycle time distribution was used as the most important criterion in this work to recur the long-term circulation of individual particles using the particle dynamics obtained from a relatively short duration of full CFD-DEM simulations.

On the intra-particle scale, the layer thickness distributions were in accordance with available data on particles from coating experiments that had been characterized by X-ray micro-computed tomography (μ-CT); the change of coefficient of variation with time was close to the analytic model. The value of the coefficient of variation of layer thickness over the particle population is much smaller than the values of individual particles. The capillary force scattered the layer thickness distributions due to its influence on RTDs. The density distributions of coating coverage at different times well followed Weibull distributions. The required $t_{cover,100}$ to achieve a completely closed coating layer on every individual particle was much longer for the simulation with capillary force. With the postulate that splashing of droplets characterized by the dimensionless number $K_d = We^{1/2}Re^{1/4}$ could produce high porosity on deposition panels, the model can predict the uniformity of porosity in the coating layer in terms of distributions of the minimum orthodromic distance L_{min} and the size of individual high porosity regions S_p. The simulation with capillary forces predicted slightly higher non-uniformity of high porosity regions for the particle population. In summary, it is important to reduce the negative effects of capillary forces on the coating process by providing enough drying capacity of the fluidization gas and by accurate control of the size distribution of spray droplets.

Further experimental research will be conducted using X-ray micro-computed tomography to access the porosity distribution of single particle coating layers.

Declaration of Competing Interest

The authors declare that they have no known competing financial interests or personal relationships that could have appeared to influence the work reported in this paper.

Acknowledgment

The authors gratefully acknowledge the funding of this work by the German Federal Ministry of Science and Education (BMBF) as part of the InnoProfile-Transfer project NaWiTec (03IPT701X) and by the German Research Foundation (DFG) as part of the priority program "Dyn-Sim-FP" (DFG-SPP 1679).

Appendix A. CFD-DEM formulations

Governing equations for particle phase

The motion of an individual particle i with mass m_i and moment of inertia I_i is calculated in a Lagrangian frame by Newton's laws of motion:

$$m_i \frac{\mathrm{d}\boldsymbol{v}_{p,i}}{\mathrm{d}t} = \boldsymbol{f}_{pf,i} + \sum_{j=1,j\neq i}^{N_1} (\boldsymbol{f}^n_{c,ij} + \boldsymbol{f}^t_{c,ij}) + \sum_{k=1,k\neq i}^{N_2} \boldsymbol{f}_{capillary,ik} + m_i\boldsymbol{g}, \tag{A.1}$$

$$I_i \frac{\mathrm{d}\boldsymbol{\omega}_i}{\mathrm{d}t} = \sum_{j=1,j\neq i}^{N_1} (\boldsymbol{T}_{t,ij} + \boldsymbol{T}_{r,ij}); \tag{A.2}$$

$\boldsymbol{v}_{p,i}$ and $\boldsymbol{\omega}_i$ are, respectively, the transitional and angular velocities of the individual particle i, N_1 is the number of particles in interaction with particle i, and N_2 is the number of liquid bridges associated with the particle i. The quantity $\boldsymbol{f}_{pf,i}$ is the particle–fluid interaction force on the particle scale; $\boldsymbol{f}^n_{c,ij}$ and $\boldsymbol{f}^t_{c,ij}$ are the particle–particle interaction forces in the normal and tangential directions; $\boldsymbol{f}_{capillary,ik}$ is the capillary force between particles induced by the liquid bridge; and $m_i\boldsymbol{g}$ is the gravitational force. The torque acting on particle i by the particle j includes two components: $\boldsymbol{T}_{t,ij}$ generated by the tangential force $\boldsymbol{f}^t_{c,ij}$, and $\boldsymbol{T}_{r,ij}$ generated by the rolling

friction. The particle–fluid interaction force $\boldsymbol{f}_{pf,i}$ mainly includes drag force $\boldsymbol{f}_{d,i}$, pressure gradient force $\boldsymbol{f}_{\nabla p,i}$, viscous force $\boldsymbol{f}_{\nabla\cdot\tau,i}$ due to fluid shear stress tensor and some other non-dominant forces $\boldsymbol{f}''$ (such as virtual mass force, Magnus force and Basset force, Crowe et al. (2011)), expressed as

$$\boldsymbol{f}_{pf,i} = \boldsymbol{f}_{d,i} + \boldsymbol{f}_{\nabla p,i} + \boldsymbol{f}_{\nabla\cdot\tau,i} + \boldsymbol{f}'', \tag{A.3}$$

in which $\boldsymbol{f}_{\nabla p,i} = -V_{p,i}\nabla p$ and $\boldsymbol{f}_{\nabla\cdot\tau,i} = V_{p,i}\nabla\cdot\boldsymbol{\tau}_f$. The drag force $\boldsymbol{f}_{d,i}$ was calculated according to Beetstra et al. (2007a,b). The non-dominant forces $\boldsymbol{f}''$ were not considered in this work.

Governing equations for fluid phase

Based on the local averaged Navier–Stokes equations, mass and momentum conservation for fluid phase are given as (Zhou et al., 2010)

$$\frac{\partial}{\partial t}(\epsilon_f\rho_f) + \nabla\cdot(\epsilon_f\rho_f\boldsymbol{u}) = 0, \tag{A.4}$$

$$\frac{\partial}{\partial t}(\epsilon_f\rho_f\boldsymbol{u}) + \nabla\cdot(\epsilon_f\rho_f\boldsymbol{u}\boldsymbol{u}) = -\epsilon_f\nabla p + \nabla\cdot(\epsilon_f\boldsymbol{\tau}_f) - \boldsymbol{F}_{pf} + \epsilon_f\rho_f\boldsymbol{g}; \tag{A.5}$$

where ϵ_f is the volume fraction of fluid, ρ_f is the density of fluid, $\boldsymbol{u}$ is the velocity of fluid, respectively. The volumetric particle–fluid interaction force $\boldsymbol{F}_{pf}$ is calculated by summation of all individual forces and dividing by the volume of the CFD cell,

$$\boldsymbol{F}_{pf} = \frac{1}{\Delta V}\sum_{i=1}^{N_3}(\boldsymbol{f}_{d,i} + \boldsymbol{f}''), \tag{A.6}$$

where N_3 is the number of particles in the CFD cell. Note that the pressure gradient force $-\epsilon_s\nabla p$ and the viscous force $\epsilon_s\nabla\cdot\boldsymbol{\tau}_f$ on particles have been separated from $\boldsymbol{F}_{pf}$ in Eq. (A.5).

Beetstra drag model

In the CFD-DEM coupling, the drag force $\boldsymbol{f}_{d,i}$ due to the fluid–solid friction at the surface of particles is calculated by the momentum exchange coefficient β_{pf}, expressed as

$$\boldsymbol{f}_{d,i} = \frac{V_{p,i}}{\epsilon_s}\beta_{pf}(\boldsymbol{u} - \boldsymbol{v}_i). \tag{A.7}$$

Simulations by the fully resolved lattice Boltzmann method (LBM) have been considered as a promising tool to derive drag models, in which the inter-phase interaction is not modeled via empirical assumptions but follows from boundary conditions at the surface of the particles. Based on extensive LBM simulations, Beetstra et al. (2007a,b) proposed a drag model for mono-disperse systems in a wide range of solid volume fractions $\epsilon_s \in [0.1, 0.6]$ and particle Reynolds numbers $Re_p \in [20, 1000]$ in the form of

$$F(\epsilon_s, Re_p) = \frac{10\epsilon_s}{\epsilon_f^2} + \epsilon_f^2(1 + 1.5\epsilon_s^{0.5}) + \frac{0.413Re_p}{24\epsilon_f^2}\left[\frac{\epsilon_f^{-1} + 3\epsilon_s\epsilon_f + 8.4Re_p^{-0.343}}{1 + 10^{3\epsilon_s}\cdot Re_p^{-(1+4\epsilon_s)/2}}\right]. \tag{A.8}$$

The relationship between normalized drag force $F(\epsilon_s, Re_p)$ and momentum exchange coefficient β_{pf} can be written as

$$\beta_{pf} = \frac{18\mu_f\epsilon_s\epsilon_f}{d_p^2}F(\epsilon_s, Re_p). \tag{A.9}$$

It is important to note that the drag force acting on the solid phase might be reduced due to the decrease of inter-phase surface for relatively large agglomerate Wang et al. (2011). Normally, the drag force can be scaled by a constant factor or a dynamic factor related to the structure of the agglomerate and the number of primary particles in the agglomerate Liu et al. (2016). In current work, the scaling of drag force was not attempted in consideration of the relatively small size and instability of the agglomerates induced by the liquid bridge.

Hertzian spring-dashpot (HSD) contact model

Two spherical particles are in mechanical contact if $(R_i + R_j - |\boldsymbol{r}_i - \boldsymbol{r}_j|) > 0$, i.e. the sum of particle radii exceeds the distance between the two centers of particles. The overlap ε_{ij} can be expressed as

$$\varepsilon_{ij} = \max\left[0, (R_i + R_j - |\boldsymbol{r}_i - \boldsymbol{r}_j|)\right], \tag{A.10}$$

The normal and tangential components of contact force can be written as

$$\boldsymbol{f}_{c,ij}^n = f_{c,ij}^n\cdot\boldsymbol{n}^n, \boldsymbol{f}_{c,ij}^t = f_{c,ij}^t\cdot\boldsymbol{n}^t; \tag{A.11}$$

where $\boldsymbol{n}^n$ and $\boldsymbol{n}^t$ are unit vectors. The normal force $f_{c,ij}^n$ changes the translational motion of particles and the tangential force $f_{c,ij}^t$ changes the rotational motion of particles. Both components of the contact force are related to the relative position of particle $\boldsymbol{r}_i - \boldsymbol{r}_j$ and the relative velocity of particles $\boldsymbol{v}_i - \boldsymbol{v}_j + (R_i\boldsymbol{\omega}_i\times\boldsymbol{n}^n + R_j\boldsymbol{\omega}_j\times\boldsymbol{n}^n)$.

In the Hertzian spring-dashpot model, stiffness coefficient (or elastic coefficient) k and the damping coefficient (or dissipative coefficient) η are used to model the conservative force f_{cons} and the dissipative force f_{dis} depending on the overlap and relative velocity, respectively. The equations used in HSD model to calculate $f_{c,ij}^n$ and $f_{t,ij}^t$ are summarized in Table A.1. The expressions for equivalent properties, including Young's modulus E_{eq}, shear modulus G_{eq}, radius R_{eq} and mass m_{eq}, can be found in the literature, for example in Jiang et al. (2018a,b). Parameters required for the simulations are the coefficient of restitution e, the friction coefficient μ_{fc}, Young's modulus E and the Poisson ratio σ.

Rolling model

The slight non-sphericity of the particles can be modelled by a rolling model that introduces an additional torque even when the relative tangential velocity at the contact point is zero. According to the work of Ai et al. (2011), the rolling friction torque $\boldsymbol{T}_{r,ij}$ can be modelled by

$$\boldsymbol{T}_r = -k_r k_n\varepsilon\frac{\boldsymbol{\omega}_r}{|\boldsymbol{\omega}_r|}R_{eq}, \tag{A.19}$$

in which k_r is a model parameter; and the relative angular velocity $\boldsymbol{\omega}_r$ is defined as

$$\boldsymbol{\omega}_r = \frac{R_i\boldsymbol{\omega}_i + R_j\boldsymbol{\omega}_j}{R_i + R_j}. \tag{A.20}$$

Table A.1
Summary of equations used in the HSD contat model.

Normal contact force f_c^n

$$f_c^n(\varepsilon, \dot{\varepsilon}) = -f_{cons}(\varepsilon) - f_{dis}(\varepsilon, \dot{\varepsilon}) = \min(0, -k_n\varepsilon - \eta_n v_{r,n}); \tag{A.12}$$

$$k_n = \tfrac{4}{3}E_{eq}\sqrt{R_{eq}\varepsilon} \tag{A.13}$$

$$\eta_n = \alpha_d(e)\sqrt{k_n m_{eq}} \tag{A.14}$$

Tangential contact force f_c^t (Coulomb frictional limit)

$$f_c^t = \begin{cases} -k_t\varepsilon_t - \eta_t v_{r,t}, & f_c^t < \mu_{fc}|f_c^n| \\ -\mu_{fc}|f_c^n|, & f_c^t > \mu_{fc}|f_c^n|; \end{cases} \tag{A.15}$$

$$k_t = 8G_{eq}\sqrt{R_{eq}\varepsilon} \tag{A.16}$$

$$\eta_t = \sqrt{\tfrac{2}{3}}\alpha_d(e)\sqrt{k_t m_{eq}} \tag{A.17}$$

Damping ratio $\alpha_d(e)$

$$\alpha_d(e) = \begin{cases} -\sqrt{5}\frac{\ln e}{\sqrt{(\ln e)^2 + \pi^2}}, & e > 0 \\ -\sqrt{5}, & e = 0 \end{cases} \tag{A.18}$$

Cohesion model

The static capillary force $f_{capillary}$, associated with the liquid bridge, can be considered as the sum of two components: 1) the surface tension acting on the three-phase contact line, and 2) the pressure difference Δp across the gas–liquid interface. Limited to the spherical shape of particles, the equation for calculating the capillary force $f_{capillary}$ associated with a liquid bridge between two particles was obtained by fitting a set of discrete solutions of the Laplace equation (Soulié et al., 2006), expressed as:

$$f_{capillary} = \pi\gamma\sqrt{R_i R_j}\left[C + \exp\left(A\frac{d_{inter}}{\max(R_i, R_j)} + B\right)\right], \tag{A.21}$$

where d_{inter} is the inter-particle distance, and γ is the surface tension. The coefficients A, B and C can be expressed as functions of the volume of liquid V_l associated with the liquid bridge, the contact angle θ (in unit of radian) and the radius of larger particle $R_{max} = \max(R_i, R_j)$:

$$A = -1.1\left(\frac{V_l}{R_{max}^3}\right)^{-0.53}, \tag{A.22}$$

$$B = \left[-0.148\ln\left(\frac{V_l}{R_{max}^3}\right) - 0.96\right]\theta^2 - 0.0082\ln\left(\frac{V_l}{R_{max}^3}\right) + 0.48, \tag{A.23}$$

$$C = 0.0018\ln\left(\frac{V_l}{R_{max}^3}\right) + 0.078. \tag{A.24}$$

It is assumed that the volume of all liquid bridges is equal and constant during the simulation (no drying effect). The rupture distance of liquid bridge can be calculated by (Lian et al., 1993)

$$D_r = (1 + 0.5\theta)\cdot V_l^{1/3}. \tag{A.25}$$

References

Ai, J., Chen, J., Rotter, J., Ooi, J., 2011. Assessment of rolling resistance models in discrete element simulations. Powder Technol. 206 (3), 269–282.

Antypov, D., Elliott, J.A., 2011. On an analytical solution for the damped Hertzian spring. EPL 94 (5), 50004.

Askarishahi, M., Salehi, M.S., Radl, S., 2017. Full-physics simulations of spray-particle interaction in a bubbling fluidized bed. AIChE J. 63 (7), 2569–2587.

Beetstra, R., van der Hoef, M., Kuipers, J.A.M., 2007a. Numerical study of segregation using a new drag force correlation for polydisperse systems derived from lattice-Boltzmann simulations. Chem. Eng. Sci. 62 (1–2), 246–255.

Beetstra, R., van der Hoef, M.A., Kuipers, J.A.M., 2007b. Drag force of intermediate Reynolds number flow past mono- and bidisperse arrays of spheres. AIChE J. 53 (2), 489–501.

Börner, M., Bück, A., Tsotsas, E., 2017. DEM-CFD investigation of particle residence time distribution in top-spray fluidised bed granulation. Chem. Eng. Sci. 161, 187–197.

Börner, M., Hagemeier, T., Ganzer, G., Peglow, M., Tsotsas, E., 2014. Experimental spray zone characterization in top-spray fluidized bed granulation. Chem. Eng. Sci. 116, 317–330.

Bück, A., Neugebauer, C., Meyer, K., Palis, S., Diez, E., Kienle, A., Heinrich, S., Tsotsas, E., 2016. Influence of operation parameters on process stability in continuous fluidised bed layering with external product classification. Powder Technol. 300, 37–45.

Cheng, X., Turton, R., 2000. The prediction of variability occurring in fluidized bed coating equipment. I. the measurement of particle circulation rates in a bottom-spray fluidized bed coater. Pharm. Dev. Technol. 5 (3), 311–322.

Crowe, C.T., Schwarzkopf, J.D., Sommerfeld, M., Tsuji, Y., 2011. Multiphase Flows with Droplets and Particles. CRC Press.

Du, Q., Faber, V., Gunzburger, M., 1999. Centroidal Voronoi tessellations: Applications and algorithms. SIAM Rev. 41 (4), 637–676.

Freireich, B., Kumar, R., Ketterhagen, W., Su, K., Wassgren, C., Zeitler, J.A., 2015. Comparisons of intra-tablet coating variability using DEM simulations, asymptotic limit models, and experiments. Chem. Eng. Sci. 131, 197–212.

Freireich, B., Wassgren, C., 2010. Intra-particle coating variability: Analysis and Monte-Carlo simulations. Chem. Eng. Sci. 65 (3), 1117–1124.

Fries, L., Antonyuk, S., Heinrich, S., Palzer, S., 2011. DEM–CFD modeling of a fluidized bed spray granulator. Chem. Eng. Sci. 66 (11), 2340–2355.

Gnielinski, V., 2010. G9 Fluid-Particle Heat Transfer in Flow Through Packed Beds of Solids. In: VDI Heat Atlas. Springer, Berlin, Heidelberg, pp. 743–744.

Goniva, C., Kloss, C., Deen, N., Kuipers, J., Pirker, S., 2012. Influence of rolling friction on single spout fluidized bed simulation. Particuology 10 (5), 582–591.

Hampel, N., Bück, A., Peglow, M., Tsotsas, E., 2013. Continuous pellet coating in a Wurster fluidized bed process. Chem. Eng. Sci. 86, 87–98.

Hede, P.D., Bach, P., Jensen, A.D., 2008. Two-fluid spray atomisation and pneumatic nozzles for fluid bed coating/agglomeration purposes: A review. Chem. Eng. Sci. 63 (14), 3821–3842.

Heinrich, S., Dosta, M., Antonyuk, S., 2015. Multiscale Analysis of a Coating Process in a Wurster Fluidized Bed Apparatus. In: Marin, G.B., Li, J. (Eds.), Advances in Chemical Engineering, vol. 46. Academic Press, pp. 83–135.

Hilton, J., Ying, D., Cleary, P., 2013. Modelling spray coating using a combined CFD–DEM and spherical harmonic formulation. Chem. Eng. Sci. 99, 141–160.

Jiang, X., Siamas, G.A., Jagus, K., Karayiannis, T.G., 2010. Physical modelling and advanced simulations of gas–liquid two-phase jet flows in atomization and sprays. Prog. Energy Combust. Sci. 36 (2), 131–167.

Jiang, Z., Bück, A., Tsotsas, E., 2018a. CFD–DEM study of residence time, droplet deposition, and collision velocity for a binary particle mixture in a Wurster fluidized bed coater. Drying Technol. 36 (6), 638–650.

Jiang, Z., Du, J., Rieck, C., Bück, A., Tsotsas, E., 2019. PTV experiments and non-spherical DEM simulations of the coefficient of restitution for irregular maltodextrin particles impacting on horizontal substrates. Powder Technol. https://doi.org/10.1016/j.powtec.2019.10.072. accepted.

Jiang, Z., Hagemeier, T., Bück, A., Tsotsas, E., 2017. Experimental measurements of particle collision dynamics in a pseudo-2D gas-solid fluidized bed. Chem. Eng. Sci. 167, 297–316.

Jiang, Z., Hagemeier, T., Bück, A., Tsotsas, E., 2018b. Color-PTV measurement and CFD-DEM simulation of the dynamics of poly-disperse particle systems in a pseudo-2D fluidized bed. Chem. Eng. Sci. 179, 115–132.

Josserand, C., Thoroddsen, S., 2016. Drop impact on a solid surface. Annu. Rev. Fluid Mech. 48 (1), 365–391.

Kieckhefen, P., Lichtenegger, T., Pietsch, S., Pirker, S., Heinrich, S., 2019. Simulation of spray coating in a spouted bed using recurrence CFD. Particuology 42, 92–103.

Knop, K., Kleinebudde, P., 2013. PAT-tools for process control in pharmaceutical film coating applications. Int. J. Pharm. 457 (2), 527–536.

Koay, C.G., 2011. Analytically exact spiral scheme for generating uniformly distributed points on the unit sphere. J. Comput. Sci. 2 (1), 88–91.

Kulju, T., Paavola, M., Spittka, H., Keiski, R.L., Juuso, E., Leiviskä, K., Muurinen, E., 2016. Modeling continuous high-shear wet granulation with DEM-PB. Chem. Eng. Sci. 142, 190–200.

Laksmana, F.L., Van Vliet, L.J., Hartman Kok, P.J.A., Vromans, H., Frijlink, H., Van der Voort Maarschalk, K., 2009. Quantitative image analysis for evaluating the coating thickness and pore distribution in coated small particles. Pharm. Res. 26 (4), 965–976.

Li, L., Rasmuson, A., Ingram, A., Johansson, M., Remmelgas, J., von Corswant, C., Folestad, S., 2015a. PEPT study of particle cycle and residence time distributions in a Wurster fluid bed. AIChE J. 61 (3), 756–768.

Li, L., Remmelgas, J., van Wachem, B.G., von Corswant, C., Johansson, M., Folestad, S., Rasmuson, A., 2015b. Residence time distributions of different size particles in the spray zone of a Wurster fluid bed studied using DEM-CFD. Powder Technol. 280, 124–134.

Lian, G., Thornton, C., Adams, M.J., 1993. A theoretical study of the liquid bridge forces between two rigid spherical bodies. J. Colloid Interface Sci. 161 (1), 138–147.

Lin, H., Dong, Y., Markl, D., Williams, B.M., Zheng, Y., Shen, Y., Zeitler, J.A., 2017. Measurement of the intertablet coating uniformity of a pharmaceutical pan coating process with combined terahertz and optical coherence tomography in-line sensing. J. Pharm. Sci. 106 (4), 1075–1084.

Liu, D., van Wachem, B.G.M., Mudde, R.F., Chen, X., van Ommen, J.R., 2016. An adhesive CFD-DEM model for simulating nanoparticle agglomerate fluidization. AIChE J. 62 (7), 2259–2270.

Lloyd, S., 1982. Least squares quantization in PCM. IEEE Trans. Inf. Theory 28 (2), 129–137.

Luo, K., Shao, C., Chai, M., Fan, J., 2019. Level set method for atomization and evaporation simulations. Prog. Energy Combust. Sci. 73, 65–94.

Meric, R.A., Erbil, H.Y., 1998. Evaporation of sessile drops on solid surfaces: Pseudospherical cap geometry. Langmuir 14 (7), 1915–1920.

Müller, D., Bück, A., Tsotsas, E., 2019. Influence of separation properties and processing strategies on product characteristics in continuous fluidized bed spray granulation. Powder Technol. 342, 572–584.

Mundo, C., Sommerfeld, M., Tropea, C., 1995. Droplet-wall collisions: Experimental studies of the deformation and breakup process. Int. J. Multiph. Flow 21 (2), 151–173.

Peglow, M., Antonyuk, S., Jacob, M., Palzer, S., Heinrich, S., Tsotsas, E., 2011. Particle Formulation in Spray Fluidized Beds. In: Tsotsas, E., Mujumdar, A.S. (Eds.), Modern Drying Technology. John Wiley & Sons Ltd, pp. 295–378.

Pei, C., Elliott, J.A., 2017. Asymptotic limits on tablet coating variability based on cap-to-band thickness distributions: A discrete element model (DEM) study. Chem. Eng. Sci. 172, 286–296.

Poozesh, S., Setiawan, N., Akafuah, N.K., Saito, K., Marsac, P.J., 2018. Assessment of predictive models for characterizing the atomization process in a spray dryer's bi-fluid nozzle. Chem. Eng. Sci. 180, 42–51.

Rajniak, P., Stepanek, F., Dhanasekharan, K., Fan, R., Mancinelli, C., Chern, R.T., 2009. A combined experimental and computational study of wet granulation in a Wurster fluid bed granulator. Powder Technol. 189 (2), 190–201.
Rieck, C., Bück, A., Tsotsas, E., 2016. Monte Carlo modeling of fluidized bed coating and layering processes. AIChE J. 62 (8), 2670–2680.
Rieck, C., Hoffmann, T., Bück, A., Peglow, M., Tsotsas, E., 2015. Influence of drying conditions on layer porosity in fluidized bed spray granulation. Powder Technol. 272, 120–131.
Rioboo, R., Marengo, M., Tropea, C., 2002. Time evolution of liquid drop impact onto solid, dry surfaces. Exp. Fluids 33 (1), 112–124.
Roberts, R.J., Rowe, R.C., York, P., 1994. The Poisson's ratio of microcrystalline cellulose. Int. J. Pharm. 105 (2), 177–180.
Schmidt, M., Bück, A., Tsotsas, E., 2017. Shell porosity in spray fluidized bed coating with suspensions. Adv. Powder Technol. 28 (11), 2921–2928.
Sondej, F., Bück, A., Koslowsky, K., Bachmann, P., Jacob, M., Tsotsas, E., 2015. Investigation of coating layer morphology by micro-computed X-ray tomography. Powder Technol. 273, 165–175.
Sondej, F., Bück, A., Tsotsas, E., 2016. Comparative analysis of the coating thickness on single particles using X-ray micro-computed tomography and confocal laser-scanning microscopy. Powder Technol. 287, 330–340.
Soulié, F., Cherblanc, F., El Youssoufi, M., Saix, C., 2006. Influence of liquid bridges on the mechanical behaviour of polydisperse granular materials. Int. J. Numer. Anal. Meth. Geomech. 30 (3), 213–228.
Suzzi, D., Radl, S., Khinast, J.G., 2010. Local analysis of the tablet coating process: Impact of operation conditions on film quality. Chem. Eng. Sci. 65 (21), 5699–5715.
Terrazas-Velarde, K., Peglow, M., Tsotsas, E., 2011. Kinetics of fluidized bed spray agglomeration for compact and porous particles. Chem. Eng. Sci. 66 (9), 1866–1878.
Turton, R., 2008. Challenges in the modeling and prediction of coating of pharmaceutical dosage forms. Powder Technol. 181 (2), 186–194.
Wang, J., van der Hoef, M.A., Kuipers, J.A.M., 2011. The role of scale resolution versus inter-particle cohesive forces in two-fluid modeling of bubbling fluidization of Geldart A particles. Chem. Eng. Sci. 66 (18), 4229–4240.
Werner, S.R.L., Jones, J.R., Paterson, A.H.J., Archer, R.H., Pearce, D.L., 2007. Air-suspension particle coating in the food industry: Part I — state of the art. Powder Technol. 171 (1), 25–33.
Yarin, A., 2005. Drop impact dynamics: Splashing, spreading, receding, bouncing. Annu. Rev. Fluid Mech. 38 (1), 159–192.
Yarin, A., Weiss, D., 1995. Impact of drops on solid surfaces: Self-similar capillary waves, and splashing as a new type of kinematic discontinuity. J. Fluid Mech. 283, 141–173.
Zhang, W., You, C., 2015. Numerical approach to predict particle breakage in dense flows by coupling multiphase particle-in-cell and Monte Carlo methods. Powder Technol. 283, 128–136.
Zhao, H., Maisels, A., Matsoukas, T., Zheng, C., 2007. Analysis of four Monte Carlo methods for the solution of population balances in dispersed systems. Powder Technol. 173 (1), 38–50.
Zhong, W., Yu, A., Liu, X., Tong, Z., Zhang, H., 2016a. DEM/CFD-DEM modelling of non-spherical particulate systems: Theoretical developments and applications. Powder Technol. 302, 108–152.
Zhong, W., Yu, A., Zhou, G., Xie, J., Zhang, H., 2016b. CFD simulation of dense particulate reaction system: Approaches, recent advances and applications. Chem. Eng. Sci. 140, 16–43.
Zhou, Z., Kuang, S., Chu, K., Yu, A., 2010. Discrete particle simulation of particle–fluid flow: Model formulations and their applicability. J. Fluid Mech. 661, 482–510.
Zhu, R., Li, S., Yao, Q., 2013. Effects of cohesion on the flow patterns of granular materials in spouted beds. Phys. Rev. E 87 (2), 022206.